

ABSTRACT

LAI, KUN-YU ALVIN. InGaN/GaN Quantum Wells Grown on Polar and Nonpolar GaN Substrates. (Under the direction of Dr. Mark Johnson and Dr. Doug Barlage).

Nonpolar (m-plane or a-plane) gallium nitride (GaN) is predicted to be a potential substrate material to improve luminous efficiencies of nitride-based quantum wells (QWs). Numerical calculations indicated that the spontaneous emission rate in a single $\text{In}_{0.15}\text{Ga}_{0.85}\text{N}/\text{GaN}$ QW could be improved by ~ 2.2 times if the polarization-induced internal field was avoided by epitaxial deposition on nonpolar substrates.

A challenge for nonpolar GaN is the limited size (less than $10 \times 10 \text{ mm}^2$) of substrates, which was addressed by expansion during the regrowth by Hydride Vapor Phase Epitaxy (HVPE). Subsurface damage in GaN substrates were reduced by annealing with NH_3 and N_2 at 950°C for 60 minutes. It was additionally found that the variation of m-plane QWs' emission properties was significantly increased when the substrate miscut toward a-axis was increased from 0° to 0.1° .

InGaN/GaN QWs were grown by Metalorganic Chemical Vapor Deposition (MOCVD) on c-plane and m-plane GaN substrates. The QWs were studied by cathodoluminescence spectroscopy with different incident electron beam probe currents (0.1 nA \sim 1000 nA). Lower emission intensities and longer peak wavelengths from c-plane QWs were attributed to the Quantum-confined Stark Effect (QCSE). The emission intensity ratios of m-plane QWs to c-plane QWs decreased from 3.04 at 1 nA to 1.53 at 1000 nA. This was identified as the stronger screening effects of QCSE at higher current densities in c-plane QWs.

To further investigate these effects in a fabricated structure, biased photoluminescence measurements were performed on m-plane InGaN/GaN QWs. The purpose was to detect the possible internal fields induced by the dot-like structure in the InGaN layer through the response of these internal fields under externally applied fields. No energy shifts of the QWs were observed, which was attributed to strong surface leakage currents.

InGaN/GaN Quantum Wells Grown on Polar and Nonpolar GaN Substrates

by
Kun-Yu Lai

A dissertation submitted to the Graduate Faculty of
North Carolina State University
in partial fulfillment of the
requirements for the Degree of
Doctor of Philosophy

Electrical Engineering

Raleigh, North Carolina

May 22nd, 2009

APPROVED BY:

Dr. Leda Lunardi

Dr. Robert M Kolbas

Dr. Ki Wook Kim

Dr. Doug Barlage
Chair of Advisory Committee

Dr. Mark Johnson
Co-Chair of Advisory Committee

DEDICATION

To my family for their never-ending support

BIOGRAPHY

Kun-Yu Alvin Lai was born in Taiwan in 1977. He received his Bachelor of Science from the department of Electrical and Control Engineering at National Chiao Tung University in 1999. In the same year, he attended the department of Electrical and Computer Engineering at University of California, Santa Barbara and received his Master of Science in 2002. In 2003, he joined in Genesis Photonics, Inc. in Taiwan and worked as a process engineer for GaN-based blue/green light emitting diodes. In 2005, he started his Ph.D. research under the supervision of Dr. Mark Johnson and Dr. Doug Barlage at North Carolina State University. His research focused on crystal growth and device analysis of InGaN/GaN quantum wells grown by metalorganic chemical vapor deposition on polar and nonpolar GaN substrates.

ACKNOWLEDGEMENTS

I am indebted to many wonderful individuals. I am thankful to my advisors Dr. Mark Johnson and Dr. Doug Barlage for their support and encouragement all the time. The completion of this degree would not be possible without their positive attitude toward my ideas and plans. My gratitude also goes to Dr. Tanya Paskova in Kyma Technologies, Inc.. The publications of this work benefits greatly from her invaluable assistance and suggestions. The comments and advice from my committee members are also highly appreciated. Additional thanks go to Joe Matthews for his great help in maintaining the equipments in the lab, and to the partners in the lab, including Ginger, Judy, Arun, Patrick, Hao, and Yi. It is their friendship that makes this lab an enjoyable place. I owe much to my parents, Bee-Sheng Lai and Wei-Wei Chang, and my sister, Chia-Chen Lai. Without their unconditional support, I would not be able to fly and study abroad. I am deeply indebted to my wife, Shiou-Ping Shiu, and my two little angles, Wei-Han and Yi-Syuan. I thank them for their accompanying and prayers from which I gain the power to pursue my dreams. Last and most importantly, I thank God. This work is done by His mercy.

TABLE OF CONTENTS

LIST OF TABLES	vii
LIST OF FIGURES	viii
Chapter 1 Introduction and Motivation	1
1.1 Background on light emitting diodes.....	1
1.2 InGaN quantum wells.....	3
1.3 Homoepitaxial growth on GaN substrates.....	6
1.4 Polarization in wurtzite GaN.....	7
1.5 Nonpolar GaN	11
1.6 Motivations and dissertation overview.....	13
1.7 Publications.....	14
Chapter 2 Preparation of GaN Substrates	16
2.1 Introduction.....	16
2.2 Experimental.....	17
2.3 Enlargement of non-polar GaN substrates by HVPE regrowth.....	20
2.4 Thermal annealing of subsurface damages in GaN substrate after polishing.....	24
2.5 Conclusions.....	31
Chapter 3 Growth of InGaN/GaN Quantum Wells on C-plane Sapphire	33
3.1 Introduction.....	33
3.2 Experimental.....	34
3.3 Results.....	36
3.4 Conclusions.....	37

Chapter 4 Effect of Substrate Miscut Angles on Nonpolar InGaN/GaN Quantum Wells.....	38
4.1 Introduction.....	38
4.2 Experimental.....	39
4.3 Results.....	40
4.4 Conclusions.....	46
Chapter 5 Polarization Effects on InGaN/GaN Quantum Wells.....	48
5.1 Introduction.....	48
5.2 Theoretical studies on Quantum-confined Stark Effect.....	49
5.3 Experimental.....	55
5.4 Results.....	56
5.5 Conclusions.....	64
Chapter 6 The Emissions of Nonpolar InGaN/GaN Quantum Wells under Biases.....	65
6.1 Introduction.....	65
6.2 Experimental.....	67
6.3 Results.....	69
6.4 Conclusions.....	73
Chapter 7 Summary and Future Works.....	74
7.1 Summaries.....	74
7.2 Future Works.....	76
Bibliography.....	81

Appendices.....	86
Appendix A MATLAB Code: Calculations of Quantum-confined Stark Effect in a Single In_{0.15}Ga_{0.85}N/GaN Quantum Well.....	87
Appendix B MOCVD Operation Procedures.....	96

LIST OF TABLES

Table 1. The two annealing conditions for GaN substrates.....	18
Table 2. Characteristics of Sample A, B, C and D measured by high-resolution XRD, AFM, and CL.....	41
Table 3. Quantum well properties of Sample A, B, C and D estimated by SIMS.....	45
Table 4. Physical parameters used in the calculations for the SER in a single InGaN/GaN quantum well.....	52

LIST OF FIGURES

Figure 1. The efficiency growth of LEDs. Figure adopted from Lumileds Lighting [9].....	3
Figure 2. Cross-sectional TEM image showing dot-like structures of InGaN layers. Figure adopted from Ref. [14].....	5
Figure 3. Free standing GaN substrates grown by HVPE. Figure adopted from Sumitomo Electric [22].....	6
Figure 4. Schematic illustration of the SP polarization in (a) zincblende GaN and (b) wurtzite GaN. The small and large spheres indicate Ga and N, respectively. The arrows indicate the directions of dipole moments, pointing from the anion (N) to the cation (Ga).....	8
Figure 5. Total electric fields (in white region) and PZ fields (in hatched region) in $Al_xIn_yGa_{1-x-y}N/GaN$ QW as a function of in-plane strain. The contact zone, indicated by the arrow, corresponds to the case of InGaN alloy. Figure adopted from Ref. [23].....	10
Figure 6. Longitudinal PZ field in strained $In_{0.1}Ga_{0.9}N/GaN$ QWs as a function of polar angle θ , defined as the angle between the growth direction and the c-axis. Figure adopted from Ref. [25].....	12
Figure 7. M-plane GaN substrate (seed) prepared by slicing from c-plane GaN boules.....	18
Figure 8. (a) Optical micrograph of the plan-view (1100) bulk GaN regrown homoepitaxially by HVPE. The vertical dark bar running through the right-half of the sample is a crack, which may be caused by the thermal constraint occurring between sapphire and GaN. (b) The micrograph in cross-section of an m-plane GaN after HVPE regrowth. The white line indicates the boundary of the substrate.....	21

Figure 9. SEM image of the cleaved cross-section perpendicular to the [0001] direction of the sample. A dashed line is drawn between the substrate and the lateral regrowth	23
Figure 10. X-ray rocking curve on the m-plane regrown surface.....	23
Figure 11. Panchromatic CL images of (a) the substrate area and (b) the regrowth area in a cleaved cross-section of an m-plane GaN after regrowth.....	23
Figure 12. (a) SEM image of Sample A before annealing. (b) Panchromatic CL image taken at the same area, revealing subsurface damages. (c) SEM image of Sample A after the annealing with $\text{NH}_3+\text{H}_2+\text{N}_2$ at 950 °C for 10 minutes. (d) Panchromatic CL image at the same area. The roughness and scratches were enhanced after annealing and became visible in SEM and CL images. (Image magnification: 500X; scale bar: 10 μm ; acceleration voltage: 5 kV).....	25
Figure 13. (a) SEM image of Sample B before annealing. (b) Panchromatic CL image at the same area, revealing subsurface damages. (c) SEM image of Sample B after the annealing with NH_3+N_2 at 950 °C for 60 minutes. (d) Panchromatic CL image at the same area, showing significantly reduced subsurface damages. (Image magnification: 500X; scale bar: 10 μm ; acceleration voltage: 5 kV).....	27
Figure 14. (a) Panchromatic CL images taken from sample at different acceleration voltages: (a) 5 kV, (b) 10 kV, (c) 15 kV, and (d) 20 kV. (Image magnification: 500X; scale bar: 10 μm).....	29
Figure 15. (a) PL spectra of sample A before and after annealing with $\text{NH}_3+\text{H}_2+\text{N}_2$. (b) PL spectra of sample B before and after annealing with NH_3+N_2	30
Figure 16. Layer structure of InGaN/GaN QWs.....	35

Figure 17. PL spectra from the optimized InGaN/GaN QWs on 2-inch c-plane sapphire.....	35
Figure 18. High-resolution XRD scans on Sample 1 and Sample 2.....	37
Figure 19. AFM image recorded on the substrate surface of Sample D.....	41
Figure 20. AFM images recorded on the QW surfaces of (a) Sample A, (b) Sample B, (c) Sample C, and (d) Sample D.....	42
Figure 21. CL spectra measured with Samples A, B, C, and D.....	44
Figure 22. In composition depth profile measured by SIMS for (a) Samples A and B and (b) Samples C and D.....	45
Figure 23. (a) The normalized SER at different of electric fields in a single In _{0.25} Ga _{0.75} N/GaN QW. (b) The emission wavelength at different electric fields from the QW.....	55
Figure 24. CL spectra taken from the QWs grown m-plane GaN, c-plane GaN and c-plane Sapphire. Probe current: 10 nA.....	57
Figure 25. Cross-sectional TEM images taken in the InGaN/GaN QWs grown on: (a) m- plane GaN, (b) c-plane GaN, and (c) c-plane sapphire.....	58
Figure 26. Normalized CL spectra at different probe currents measured on: (a) m-plane GaN, (b) c-plane GaN, and (c) c-plane sapphire.....	58
Figure 27. CL Peak wavelengths at different probe currents for QWs on c-GaN and m-GN.	60
Figure 28. (a) The integrated CL emission intensities of the QWs on m-GaN and c-GaN at different CL probe currents. (b) The integrated CL intensity ratios of the QWs on m-GaN and c-GaN, defined as $R = I_m / I_c$, at different CL probe currents.....	61
Figure 29. Schematic illustration of m-plane and c-plane QWs at low and high probe currents.....	63
Figure 30. Schematic illustration of biased microPL measurement set-up.....	68

Figure 31. Schematic showing the relevant position of laser beam spot on the surface of m-plane QWs. Dimensions are not to scale.....	69
Figure 32. Micro-PL spectra from m-plane InGaN/GaN QWs under different DC bases.....	70
Figure 33. Simulated lateral electric field distribution within the 1.2 μm gap of adjacent contacts under a DC bias of 30 V.....	71
Figure 34. (a) Biased microPL spectra of a single InGaN layer grown on c-plane sapphire recorded at 4.2 K. (b) Plots of peak intensities and energies as a function of biases in (a). Figure adopted from Ref. [55].....	72
Figure 35. Layer structure of the 3 rd -generation sample for biased microPL measurement....	77
Figure 36. PL spectra of the InGaN/GaN QWs grown on sapphire at the growth temperature of (a) 750°C and (b) 730°C. The peaks at 362 nm were from the near-band-edge emission of GaN.....	79
Figure 37. PL spectra of the InGaN/GaN QWs grown on sapphire at the TMIn flow of (a) 38 sccm and (b) 45 sccm.....	80

CHAPTER 1

Introduction and Motivation

1.1 Background on light emitting diodes

Visible spectrum (red) light emitting diodes (LEDs) debuted in 1962 [1]. The invention was followed by the first demonstration of yellow LED in 1972 [2]. Due to the limited light emission efficiency, red and yellow LEDs were initially used in wrist watches and instrument panel indicators. Until early 1990s, LEDs operating in this portion of spectrum did not achieve the light efficiencies superior to those of incandescent lamps [3]. Although the first blue LED was made in 1971 [4], it has proved difficult to extend the wavelength to the range below 550 nm. In the following decade, blue LEDs were of little practical use because of the low efficiencies. Due to the lack of blue spectrum, the applications of LEDs were limited mostly to electronic indicators.

The main challenges to short wavelength LEDs were attributed to the growth problems of wide band gap semiconductors: 1) lack of suitable substrates, and 2) difficulties in making

p-doped materials. With the problems unresolved, wide band gap semiconductors can only be grown on foreign substrates, resulting in low quality crystals due to the mismatch in lattice constants and thermal expansion coefficients. Furthermore, the lack of p-doped semiconductors made it impossible to fabricate electronically driven devices.

The key breakthrough came in late 1980s. Specular and crack-free GaN films were eventually achieved with low temperature AlN or GaN buffer layers grown by metalorganic chemical vapor deposition (MOCVD) [5,6]. P-type GaN was obtained by Mg doping of MOCVD films with a low energy electron beam irradiation (LEEBI) treatment [7], and soon it was found that thermal annealing at 700 °C under N₂ ambient led to similar results [8]. The success in producing high quality GaN films made it possible to grow InGaN quantum wells (QWs), the key components to emit light with the wavelength below 550 nm. The applications of solid state lighting advanced dramatically since the commercialization of blue LEDs in mid 1990s. With the three primary colors available, white light sources can be made either with proper mixtures or with the combination of blue LEDs and yellow phosphors. This opens up many important applications, such as large panel displays, outdoor signs or even general lighting. Figure 1 shows the efficiency growth of LEDs. The rapid development of technology has caused the light output to double about every 36 months since the 1960s, in a similar way to Moore's law. Now, with the advantages of low turn-on voltage, small size and long lifetime, solid state lighting is of even more importance as energy conservation has become a global challenge. It is the primary goal of this project to first understand how GaN-based LEDs are affected by some inherent material properties, and secondly, to develop the technology for the devices with superior performances.

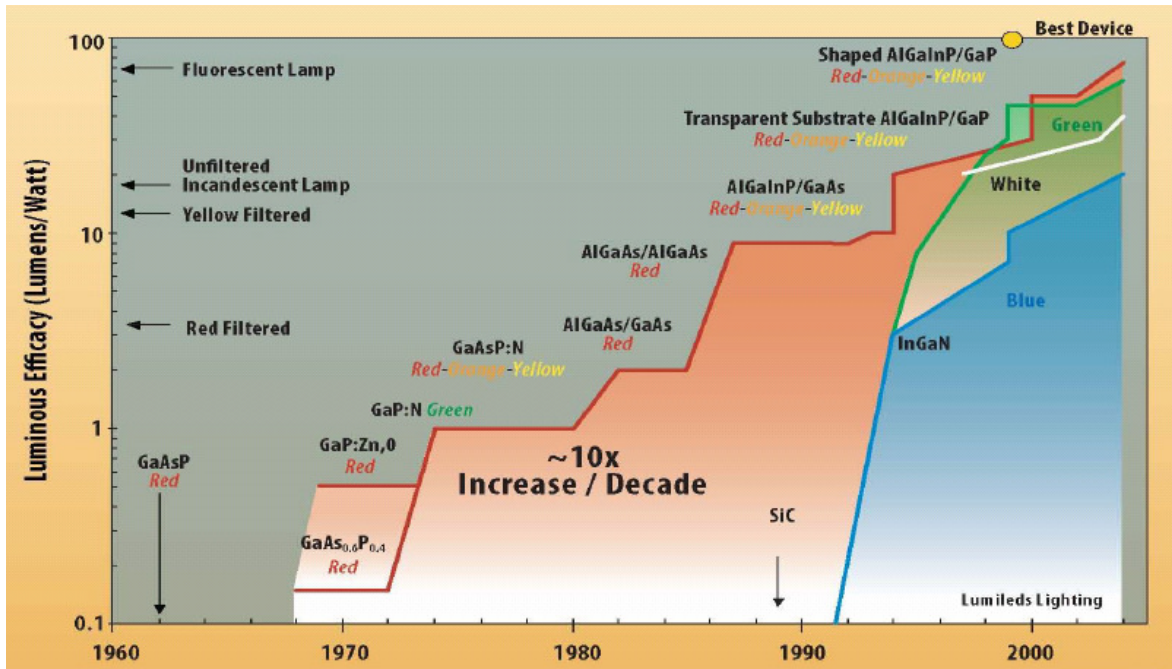


Figure 1. The efficiency growth of LEDs. Figure adopted from Lumileds Lighting [9].

1.2 InGaN quantum wells

Since the commercialization of blue LEDs, GaN has become one of the most important semiconductors in the post-silicon age. Depending on the compositions, the bandgap energy of AlInGaN varies from 6.2 eV to 0.7 eV. The large energy variation and direct band gaps make AlInGaN a candidate for light emitting devices. However, the success of III-nitrides was not expected in the early stage of development. Before 1990, most of the research efforts on wide-bandgap semiconductor were involved in II-VI compounds (ZnSe/ZnS) because of the less lattice mismatch. Indeed, now people are still amazed at the high luminescence efficiencies achieved by InGaN QWs.

The lattice mismatch between GaN and sapphire, the main substrate for commercial LEDs, is 13% [10]. The huge mismatch resulted in a high density of structural defects. Typical threading dislocation densities in commercial blue LEDs observed by transmission electron microscopy (TEM) were on the order of 10^{10} cm⁻² [11]. Dislocation densities in this range would not be allowed in a working device fabricated with other materials. Being responsible for the high efficiencies in blue and green emissions, InGaN QWs' immunity to the structural defects drew much research attention in the last decade. Up to now, it is believed that the luminescence in blue/green LEDs came from the radiative recombination within the In-rich regions, acting as quantum dot (QD)-like structures due to the phase segregation in InGaN layers. Phase segregation in InGaN alloys can be attributed to the low miscibility of InN in GaN [12]. Theoretical and experimental results suggested that the QD-like structures confined the carriers not only vertically (along the growth direction) but also laterally so that the diffusion towards the surrounding defects was suppressed [13-16].

Cross-sectional TEM and energy-dispersive x-ray (EDX) microanalysis, observed by Narukawa *et al.* [14], showed that the contrast of light and shade in the InGaN well layers corresponds to the difference in In composition. Figure 2 shows the dot-like structures of InGaN layers revealed by the cross-sectional TEM image. It was argued that the self-formed QD-like structures may not be due to the interface fluctuation, but result from the intrinsic nature of InGaN alloys since phase separation would be energetically favored in this system. Electroluminescence and photocurrent spectra of commercial LEDs, measured by O'Donnell *et al.* [15], also suggested that the scalabilities of the Stokes shift, absorption edge

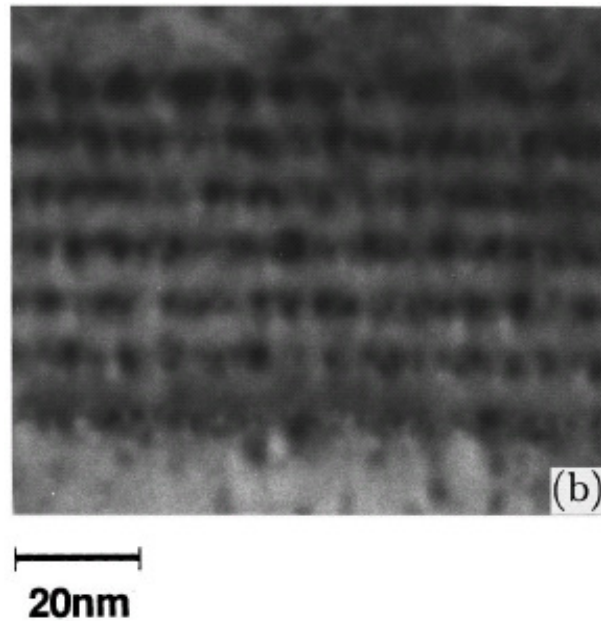


Figure 2. Cross-sectional TEM image showing dot-like structures of InGaN layers. Figure adopted from Ref. [14].

broadening, and luminescence peak width with emission peak energy revealed a common factor controlling the spectroscopic properties of InGaN layers. It was proposed that this commonality arise from the presence of quantum dots whose composition did not change with the level of indium incorporation. Carriers excited optically or electrically were captured by the quantum dots before they can be destroyed in the network of dislocations.

1.3 Homoepitaxial growth on GaN substrates

The desire to further improve device performance drove people to grow III-nitride films on native GaN substrates. Most of the commercially available nitride-based devices are grown on sapphire or SiC substrates. The mismatches in lattice constants and thermal expansion coefficients between the substrates and the epitaxial films result in undesired defects, such as threading dislocations [17] or cracks [18]. Compared with those built on sapphire, devices fabricated homoepitaxially on GaN substrates have exhibited superior performances [19-20]. Due to the scalability and the high growth rates (up to several hundred microns per hour), hydride vapor phase epitaxy (HVPE) is currently one of the most promising techniques to produce bulk GaN substrates. The development of bulk GaN is still in the early stage, and several critical problems remain to be resolved. Difficulty in obtaining large-size substrates is one of the main challenges. Currently, 2-inch free standing GaN substrates are only available for mass production by growing bulk GaN on GaAs substrates by HVPE and remove the GaAs substrates by aqua regia [21]. Figure 3 shows the image of GaN substrate grown by HVPE. In order to reduce the cost and the availability, alternative methods are desired.



Figure 3. Free standing GaN substrates grown by HVPE. Figure adopted from Sumitomo Electric [22].

1.4 Polarization in wurtzite GaN

Epilayers for conventional III-nitride devices are grown along the polar [0001] direction and preserve wurtzite structures. The lack of inversion symmetry in wurtzite structure leads to spontaneous (SP) polarization [23], and the lattice mismatch between epilayers and substrates results in piezoelectric (PZ) polarization [24]. These two polarizations were found to induce huge electric fields up to 15 MV/cm along the [0001] direction in wurtzite III-nitrides [23]. These substantial electric fields pull the electrons and holes towards opposite sides in quantum wells, resulting in the reduced overlap between wave functions. The reduced overlap adversely affects GaN-based optical devices in 2 ways: i) decreasing the radiative recombination efficiencies [25]; ii) shifting the emission to shorter wavelengths (blue-shift) with increased driving currents, as a result of Quantum-confined Stark Effect [26,27].

In electromagnetics, polarization vector \mathbf{P} is defined as the dipole moment per unit volume:

$$\mathbf{P} = \lim_{V \rightarrow 0} \left[\frac{\mathbf{p}_t}{V} \right] \text{ (C/m}^2\text{)} \quad (1-1)$$

where V is a volume, \mathbf{p}_t is the total number (N) of dipole moments in V :

$$\mathbf{p}_t = \sum_{i=1}^N d\mathbf{p}_i \quad (1-2)$$

where $d\mathbf{p}_i$ is a single dipole moment given by $d\mathbf{p}_i = Ql_i$, where Q is the magnitude (in coulombs, C) of each of the negative and positive charges whose centroids are displaced vectorially by distance l_i .

SP polarization is defined as the polarization in the absence of strain, and can be explained with Figure 4. In Figure 4 (a), the four polar axes in zincblende GaN cancel each other in direction and in magnitude. As a result, no SP polarization is induced. However, this is not the case for wurtzite GaN. As shown in Figure 4 (b), the lack of inversion symmetry in wurtzite structure leads to the unbalanced polar axes. The resulting SP polarization is in the direction of $[0001]$.

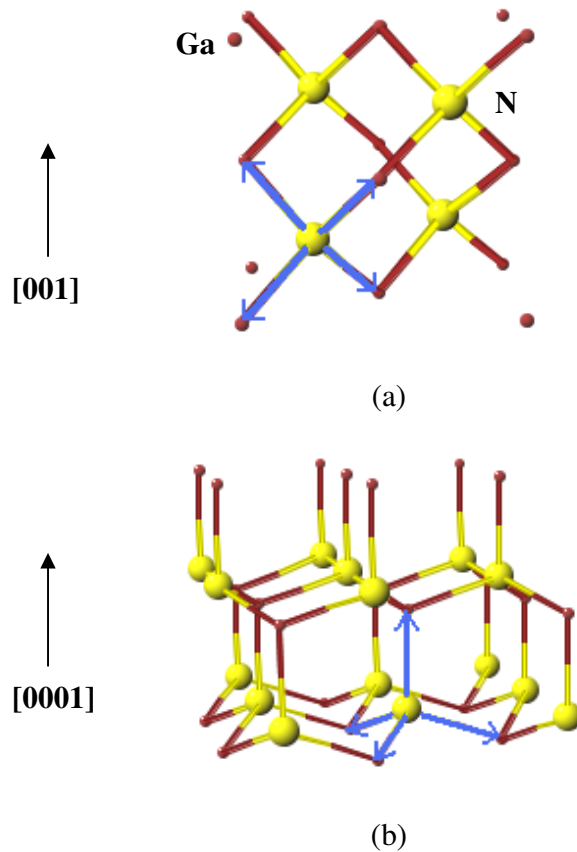


Figure 4. Schematic illustration of the SP polarization in (a) zincblende GaN and (b) wurtzite GaN. The small and large spheres indicate Ga and N, respectively. The arrows indicate the directions of dipole moments, pointing from the anion (N) to the cation (Ga).

PZ polarization is related to strain by

$$\begin{pmatrix} \mathbf{p}_x^{pz} \\ \mathbf{p}_y^{pz} \\ \mathbf{p}_z^{pz} \end{pmatrix} = \begin{pmatrix} 0 & 0 & 0 & 0 & e_{15} & 0 \\ 0 & 0 & 0 & e_{15} & 0 & 0 \\ e_{31} & e_{31} & e_{33} & 0 & 0 & 0 \end{pmatrix} \cdot \begin{pmatrix} \varepsilon_{xx} \\ \varepsilon_{yy} \\ \varepsilon_{zz} \\ \varepsilon_{yz} \\ \varepsilon_{zx} \\ \varepsilon_{xy} \end{pmatrix} \quad (1-3)$$

where \mathbf{p}_x^{pz} , \mathbf{p}_y^{pz} , and \mathbf{p}_z^{pz} are the PZ polarizations in every direction, e_{ij} ($i, j = x, y, z$) is the PZ constant, and ε_{ij} is strain in the strained layer. The z direction is set parallel to the [0001] axis. The PZ constants, e_{31} and e_{33} , correspond to the polarization along the c -axis, while e_{15} is related to that induced by a shear strain. Therefore, in the calculation of the electric field along the c -axis, e_{15} is often omitted. The strain elements in the case of a wurtzite structure are

$$\begin{aligned} \varepsilon_{xx} = \varepsilon_{yy} &= \frac{a_s - a_e}{a_e} \\ \varepsilon_{zz} &= -\frac{2c_{13}}{c_{33}} \cdot \varepsilon_{xx} \\ \varepsilon_{yz} = \varepsilon_{zx} = \varepsilon_{xy} &= 0 \end{aligned} \quad (1-4)$$

where a_e and a_s are respectively the free-standing a -axis lattice constants of the epitaxial layer and the substrate, c_{13} and c_{33} are the elastic stiffness constants for the epitaxial layer.

The total polarization \mathbf{P} in wurtzite GaN is sum of PZ and SP polarizations: $\mathbf{P} = \mathbf{P}^{pz} + \mathbf{P}^{sp}$. Polarization is related to electric field \mathbf{E} by elementary electrostatics: $\mathbf{D} = \varepsilon\mathbf{E} + \mathbf{P}$, where \mathbf{D} is the displacement field, and ε is the static dielectric constant. Bernardini *et al.* calculated

the total polarization in III-Nitrides by applying Vegard interpolation to SP polarization and PZ constants, and assuming a uniform displacement field all over the crystal [23]. Figure 5 presents the values of the electric field as a function of strain in a single $\text{Al}_x\text{In}_y\text{Ga}_{1-x-y}\text{N}$ QW with GaN barriers. The white region corresponds to the values of total electric fields ($\mathbf{E} = \mathbf{E}^{\text{PZ}} + \mathbf{E}^{\text{SP}}$), while the hatched region corresponds to those purely by PZ polarization (\mathbf{E}^{PZ}). In the figure, it can be seen that huge electric field, up to 15 MV/cm, is expected in the alloy of InGaN with high In compositions. Figure 5 also shows that SP polarization is dominant in Al-rich alloy wells, while PZ polarization is dominant in In-rich regions.

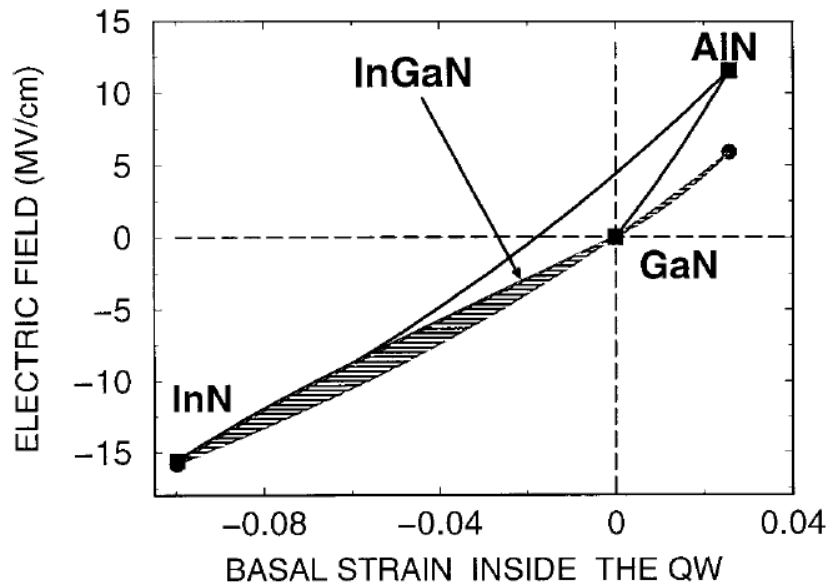


Figure 5. Total electric fields (in white region) and PZ fields (in hatched region) in $\text{Al}_x\text{In}_y\text{Ga}_{1-x-y}\text{N}/\text{GaN}$ QW as a function of in-plane strain. The contact zone, indicated by the arrow, corresponds to the case of InGaN alloy. Figure adopted from Ref. [23].

1.5 Nonpolar GaN

In the late 1990s, the results from theoretical calculations indicated the undesired internal electrical fields could be avoided by growing QWs along the directions of $[1\bar{1}00]$ and $[11\bar{2}0]$ [23, 25]. Nonpolar GaN was then referred as the crystal with the fabrication surface of m-plane $\{1\bar{1}00\}$ or a-plane $\{11\bar{2}0\}$. Figure 6 shows the calculated PZ fields in the strained $\text{In}_{0.1}\text{Ga}_{0.9}\text{N}/\text{GaN}$ QWs as a function of θ , defined as the angle between the growth direction and the c-axis [25]. In the figure, it is shown that no PZ field is induced in the case of $\theta = 39^\circ$ and $\theta = 90^\circ$. Examples of the crystal orientations are $(11\bar{2}4)$ and $(10\bar{1}2)$ for $\theta = 39^\circ$, and $(11\bar{2}0)$ and $(1\bar{1}00)$ for $\theta = 90^\circ$.

Building devices on nonpolar GaN has drawn much research interest since her potential was proposed. However, III-nitrides layers heteroepitaxially grown on nonpolar substrates, such as $\gamma\text{-LiAlO}_2$ [28] or r-plane sapphire [29] consistently show high densities of stacking faults, in addition to dislocations which are commonly observed in c-plane III-nitrides. These stacking faults and dislocations adversely affect the optical devices in blue and UV regions [30]. To overcome this problem, nonpolar substrates can be synthesized by growing thick c-plane GaN by HVPE, and then slicing transversely to expose nonpolar surfaces. Nonpolar substrates obtained in this manner have been proven to possess superior structural and optical qualities compared to those obtained heteroepitaxially [31]. Optical devices built on transversely exposed (TE) nonpolar GaN substrates also showed dramatically improved performances [32, 33]. In this study, InGaN/GaN QWs grown on TE m-plane GaN substrates are characterized by various techniques. The results are compared with those reported previously, and explanations for the difference are provided.

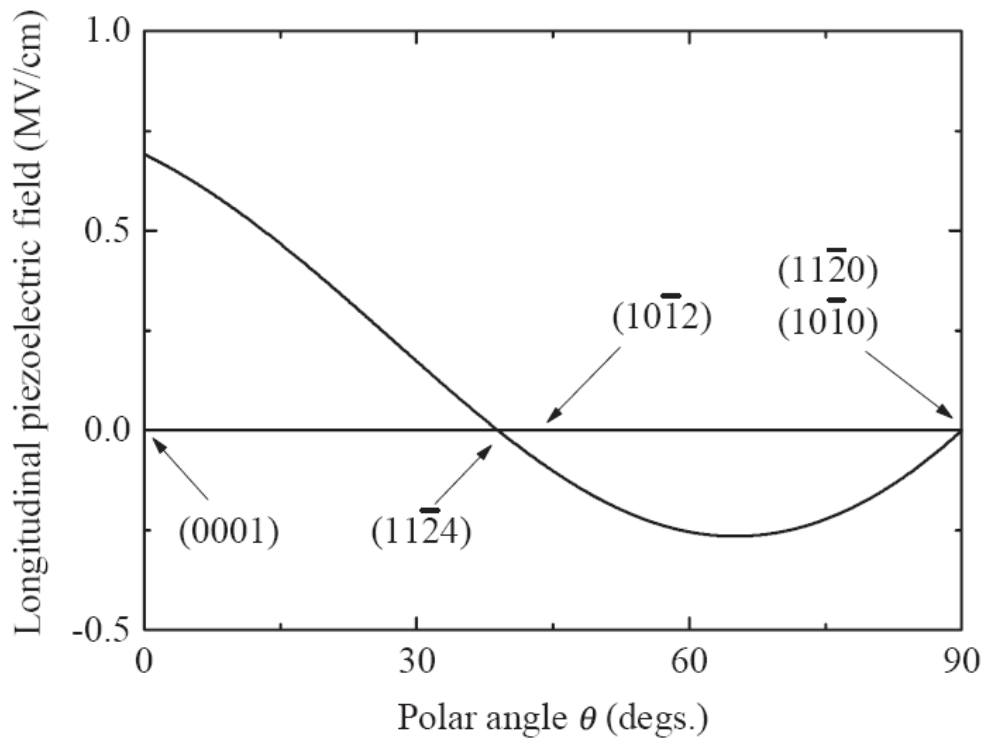


Figure 6. Longitudinal PZ field in strained $\text{In}_{0.1}\text{Ga}_{0.9}\text{N}/\text{GaN}$ QWs as a function of polar angle θ , defined as the angle between the growth direction and the c -axis. Figure adopted from Ref. [25].

1.6 Motivations and dissertation overview

The purpose of this project is to evaluate the effect of polarization on wurtzite InGaN/GaN QWs. This requires the optimization work on substrate preparation and QWs growth. With the optimization work completed, analyses can be performed to understand how the properties of QWs are affected by the polarization-induced electrical fields. The dissertation is organized as follows:

Chapter 2 described the preparation of GaN substrates. The procedures for making polar and nonpolar GaN substrates are provided. The substrates are characterized by different techniques in order to evaluate the crystal qualities. Methods to improve the substrates' properties are presented.

Chapter 3 contains the results of InGaN/GaN QWs grown on c-plane sapphire. The QWs structures are grown by metal-organic chemical vapor deposition (MOCVD). Details of the optimized growth conditions are provided. The method of evaluating well/barrier thickness by x-ray diffraction is described.

Chapter 4 provides the study of substrate miscut effects on nonpolar InGaN/GaN QWs. QWs grown on the GaN substrates with different miscut angles are systematically compared. The mechanism responsible for the different properties, including surface smoothness, emission intensities, and peak wavelengths are proposed.

Chapter 5 presents the evaluation results of polar and nonpolar InGaN/GaN QWs. The evaluation consists of theoretical and experimental parts. In theoretical part, stationary perturbation theory is employed to study quantum-confined Stark effect (QCSE) in a single

InGaN/GaN QW. After the analysis, experimental results obtained from the QWs grown on polar and nonpolar GaN are provided and compared with results by theory.

Chapter 6 contains the study of QCSE in nonpolar InGaN/GaN QWs. The purpose of this study is to investigate the potential electrical field induced by the polarization existing in the dot-like structures of m-plane InGaN layers. The emission spectra of m-plane QWs under lateral DC biases are presented. Problems of the measurements are discussed.

Chapter 7 summarizes the results of this project, and proposes the plan for future work.

1.7 Publications

In Preparation:

1. “Comparison of InGaN/GaN quantum wells grown on m-plane GaN substrate and c-plane sapphire”, K.Y. Lai, M.A.L. Johnson, T. Paskova, V.D. Wheeler, J.A. Grenko, K. Udvary, E.A. Preble, and K.R. Evans, to be submitted to *Journal of Crystal Growth*, 2009
2. “Changes in emission efficiencies of m-plane and c-plane InGaN/GaN quantum wells with increasing cathodoluminescence injection currents”, K.Y. Lai, M.A.L. Johnson, D.W. Barlage, T. Paskova, K. Udvary, E.A. Preble, and K.R. Evans, reviewed by *Applied Physics Letters*, 2009.
3. “Effect of m-plane GaN substrate miscut on InGaN/GaN quantum well growth”, K.Y. Lai, M.A.L. Johnson, T. Paskova, V.D. Wheeler, J.A. Grenko, K. Udvary, E.A. Preble, and K.R. Evans, reviewed by *Applied Physics Letter*, 2009.

Published:

1. “Cathodoluminescence evaluation of subsurface damage in GaN substrate after polishing”, K.Y. Lai, M.A.L. Johnson, T. Paskova, A.D. Hanser, K. Udvary, E.A. Preble, and K.R. Evans, *Phys. Stat. Sol. (c)*. **6**, S325, 2009.
2. “Enlargement of bulk non-polar GaN substrates by HVPE regrowth”, K.Y. Lai, V.D. Wheeler, J.A. Grenko, M.A.L. Johnson, A.D. Hanser, E.A. Preble, L. Liu, T. Paskova, and K.R. Evans, *Phys. Stat. Sol. (c)* **5**, 1886, 2008.
3. “Characterization of Non-Polar Surfaces in HVPE Grown Gallium Nitride”, Kun-Yu Lai, Judith A. Grenko, V.D. Wheeler, Mark Johnson, E.A. Preble, N. Mark Williams, and A.D. Hanser, *Mater. Res. Soc. Symp. Proc.* **955**, 0955-109-05, 2007.

CHAPTER 2

Preparation of GaN Substrates

2.1 Introduction

Native bulk GaN grown by HVPE is currently one of the best substrates for nitride-based devices. As mentioned in sections 1.3 and 1.5, HVPE-grown polar and nonpolar GaN substrates have led to superior device performances. However, some challenges still remain to be overcome. Substrate size is the main difficulty, especially for nonpolar GaN. Although nonpolar GaN obtained by slicing from c-plane GaN boules produce promising crystal qualities, the very limited substrate sizes prevent her from being commercialized through mass production.

Surface preparation is another issue. During the process of making GaN substrates, surface preparation is of critical importance for subsequent device fabrication. Grinding, lapping, and polishing are the typical processes used to prepare the substrate and its surface. There are three important characteristics that require special attention as the criteria for epitaxial ready surface: i) smoothness, ii) scratches, and iii) subsurface damages. The latter is

especially critical since it is unobservable by the standard optical, atomic force and scanning electron microscopy techniques. Subsurface damages were believed to be caused by the unbalanced force of the silica-colloid grinding during the process of surface polish. Cathodoluminescence is one of the techniques being able to reveal the subsurface damages by measuring the optical intensity within the interaction volume of the incident electron beams. If present, subsurface damages can lead to sub-optimal properties of epitaxial films and heterostructures grown thereupon [34]. Thermal annealing has been adopted as an effective approach to recover the surface damage in GaN substrates induced by mechanical polish. Enhanced near-band-edge emissions and higher flatness of the surface were obtained after annealing [35]. However, little work has been accomplished to investigate the effects of thermal annealing on subsurface damages.

In this chapter, a method to enlarge bulk non-polar GaN is investigated. Non-polar m-plane GaN substrates were regrown homoepitaxially by HVPE with the attempt to achieve high lateral expansion rates. In order to remove subsurface damages, different annealing conditions were applied to GaN substrates after polish. The goal is to develop an optimum process for the preparation of HVPE GaN substrates.

2.2 Experimental

Bulk non-polar GaN was prepared by Kyma Technologies, Inc., and the procedures are described as follows: a GaN boule, 2-inch in diameter and 9-mm in thickness, was grown on c-plane sapphire by HVPE. After removing the sapphire substrate, the GaN boule was cut transversely (along the c-axis) to expose m-plane surfaces $\{1\bar{1}00\}$.

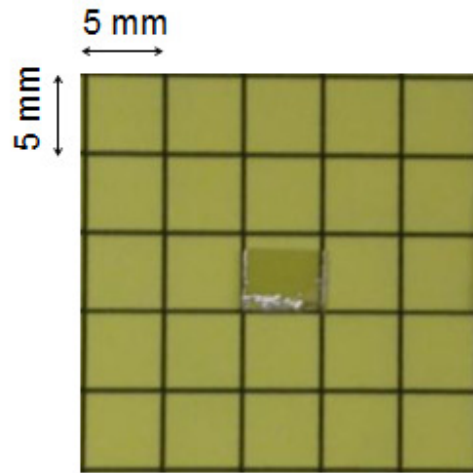


Figure 7. M-plane GaN substrate (seed) prepared by slicing from c-plane GaN boules.

Table 1. The two annealing conditions for GaN substrates.

	Sample A	Sample B
Temperature	950 °C	950 °C
Gases	NH3: 4000 sccm N2: 5000 sccm H2: 7700 sccm	NH3: 4000 sccm N2: 12700 sccm H2: 0 sccm
Pressure	76 Torr	76 Torr
Temp. Ramp Rate	120 °C/min	120 °C/min
Time	10 minutes	60 minutes

The exposed non-polar surface was polished mechanically and chemically to obtain high flatness. Then an m-plane seed with approximate size of $8 \times 4 \text{ mm}^2$ was obtained by manually cleaving. Figure 7 shows the image of an example m-plane GaN seed thus prepared. Finally, the seed was placed on the sapphire support plate, and loaded into the HVPE chamber for regrowth. As the regrowth started, the position of seed was fixed by the surrounding GaN directly grown sapphire. The regrowth time was 2 hours at the regrowth condition optimized for the growth in [0001] direction and expected to result in 500- μm -thick overgrown layer.

The regrown sample was characterized by optical microscopy, scanning electron microscopy (SEM), x-ray diffraction (XRD) and cathodoluminescence (CL). The XRD was measured with a Cu anode at 40 keV and 45 mA. The SEM/CL images were obtained with the acceleration voltage of 5kV and the probing current of 0.6 nA.

In order to reduce the subsurface damages in GaN substrates, thermal treatments with different conditions were carried out in the reactor of an MOCVD system. Since the annealing with N_2 or N_2 plasma treatment was reported to produce smoother surface [35], while the annealing with H_2 tended to result in rougher surface [57], thermal annealing with different gas mixtures were tested in order to compare the surface morphologies and the effects on subsurface damages. Two samples (A and B) grown under different conditions [38], but with identical polishing procedure were annealed at different gas conditions: Sample A was annealed with the gas mixture of NH_3 , H_2 and N_2 , while Sample B was annealed with the mixture of NH_3 and N_2 . Details of the two annealing conditions were summarized in Table 1. Before annealing, the crystalline qualities of Sample A and Sample B

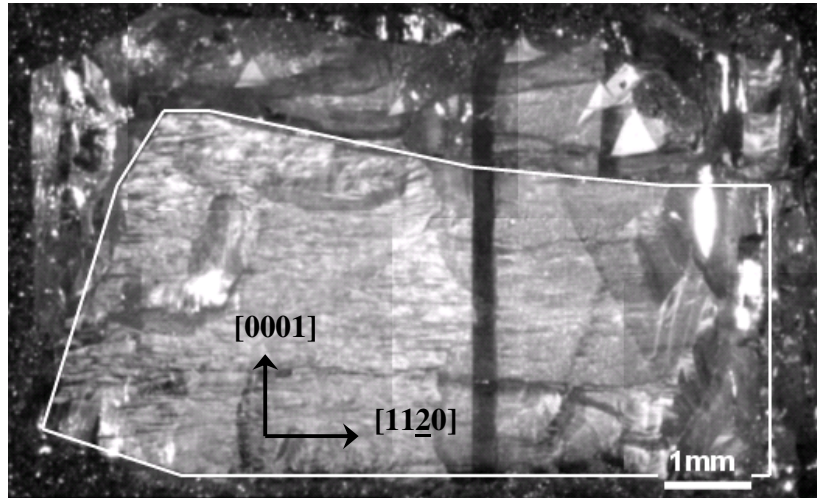
was measured by X-ray rocking curves. The full widths at half maximum (FWHMs) for GaN (0002) from Sample A and Sample B were 189 arc seconds and 372 arc seconds, respectively.

SEM and panchromatic CL imaging, with accelerating voltages of 5-20 kV and probing current of 0.6 nA, were used to characterize the surface morphology and subsurface damage. Photoluminescence (PL) spectroscopy, performed with He-Cd laser excitation at 325nm at room temperature was used to study the optical properties. Atomic force microscopy (AFM) with the scanning area of $10 \times 10 \mu\text{m}^2$ was employed to evaluate surface roughness.

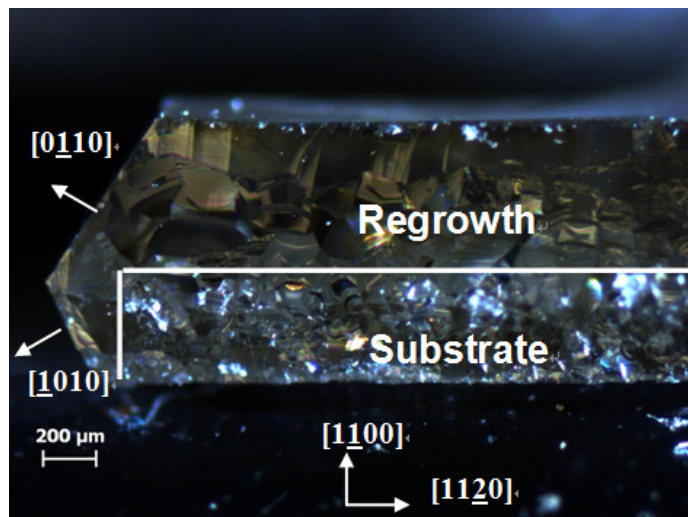
2.3 Enlargement of non-polar GaN substrates by HVPE regrowth

Figure 8 (a) presents the optical micrograph showing a plan-view of m-plane bulk GaN after HVPE regrowth with 2 hours. Firstly, it is found that the substantial lateral expansion occurred in $[0001]$, $[11\bar{2}0]$ and $[\bar{1}120]$. In these three directions, the thickness of lateral expansion was at least 500 μm . The interfaces between the seed and the regrown crystal were indicated by the white line. The non-straight interfaces were from the irregularity in cleaving during seed preparation. Secondly, since very little lateral expansion was observed in bottom of the sample, the regrowth rate is believed to be much higher in $[0001]$ than that in $[000\bar{1}]$. Since the formation of GaN in an HVPE system is dominated by the consumption of GaCl with H_2 or NH_3 [36], the growth rate on the (0001) Ga polar surface should be much higher than that on the (000 $\bar{1}$) N polar surface.

Figure 8 (b) shows a micrograph in cross-section of an m-plane GaN sample regrown at similar growth conditions. In the figure, the substrate and the regrowth can be



(a)



(b)

Figure 8. (a) Optical micrograph of the plan-view ($1\bar{1}00$) bulk GaN regrown homoepitaxially by HVPE. The vertical dark bar running through the right-half of the sample is a crack, which may be caused by the thermal constraint occurring between sapphire and GaN. (b) The micrograph in cross-section of an m-plane GaN after HVPE regrowth. The white line indicates the boundary of the substrate.

differentiated by the surface morphology, namely the substrate area is rougher; while the regrowth area is smoother. More importantly, it was found that the crystal was regrown predominantly in the m directions $\langle 1\bar{1}00 \rangle$, as the angles between any two facets were all identified to be 120° . This observation indicates that the m -plane is one of the preferential expansion planes during the regrowth.

In order to observe the crystal closely, the sample was cleaved along the top edge of the sample shown in Figure 8 (a) and evaluated by SEM. Figure 9 shows a SEM micrograph of the cross-section perpendicular to the $[0001]$ direction of the sample. The contrast difference unambiguously defines the substrate region and the regrowth region. A dashed line was drawn along the interface. Lateral regrowth of $836 \mu\text{m}$ in the $[\bar{1}120]$ direction was measured, corresponding to a growth rate of $418 \mu\text{m/h}$.

The structural quality of the regrown crystal was evaluated by XRD and CL imaging. The single crystalline of the regrown crystal was confirmed by XRD measurement. Figure 10 shows the high resolution rocking curve on the m -plane surface of the sample after regrowth. The full-width at half maximum (FWHM) of the rocking curve was approximately 116 arcsec , indicating a high quality of the regrowth. In order to compare the dislocation densities in the seed and in the regrown crystal, CL images were taken at the cleaved c -plane cross-section of an m -plane sample after regrowth.

Figure 11 (a) and (b) present the panchromatic CL images taken from the seed and the regrown areas, respectively. The dislocation density in the seed was approximately $5 \times 10^6 \text{ cm}^{-2}$, while that in the regrown areas is approximately $1 \times 10^6 \text{ cm}^{-2}$. The seemingly lower

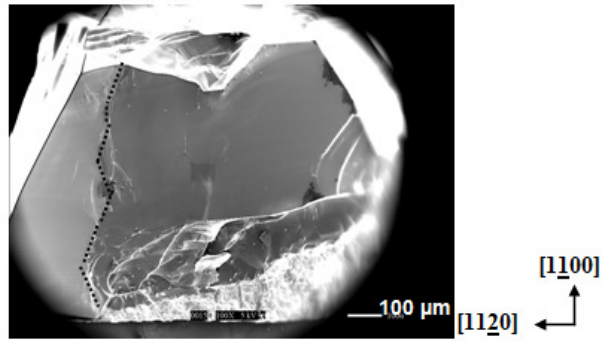


Figure 9. SEM image of the cleaved cross-section perpendicular to the [0001] direction of the sample. A dashed line is drawn between the substrate and the lateral regrowth.

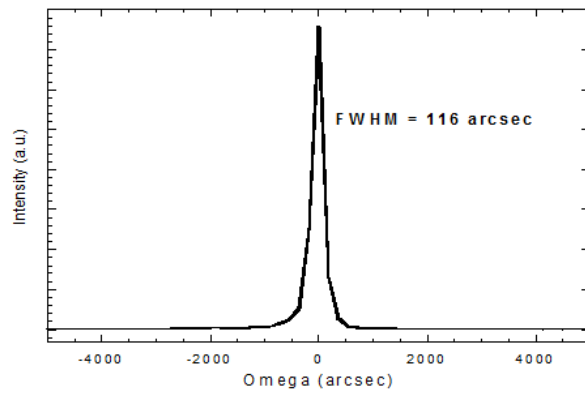


Figure 10. X-ray rocking curve on the m-plane regrown surface.

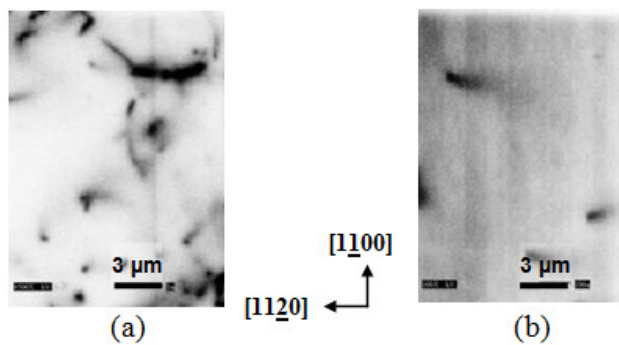


Figure 11. Panchromatic CL images of (a) the substrate area and (b) the regrowth area in a cleaved cross-section of an m-plane GaN after regrowth.

dislocation density in the regrowth area indicates that the quality of non-polar GaN does not deteriorate after regrowth.

2.4 Thermal annealing of subsurface damages in GaN substrate after polishing

Figures 12 (a) – (d) present the SEM and CL images of Sample A (describe on page 15) before and after annealing. Figure 12 (a) shows that the polished surface (before annealing) possessed a very smooth surface. AFM measurement confirmed the smoothness by giving the RMS roughness of 0.12 nm. However, the panchromatic CL image taken at the same area, shown in Figure 12 (b), revealed additional lines with lower emission intensity identified as subsurface damages. Figure 12 (c) and (d) show the results after the annealing with NH₃, H₂ and N₂ at 950 °C for 10 minutes. It is apparent that the scratches become more prevalent, and were even observed in the SEM image. The surface roughness also increased after annealing. The RMS roughness of the annealed surface went up to 11.83 nm. This result indicates that the annealing with H₂-containing gas mixtures produced an inhomogeneous etching effect on the surface, and enhanced the damages caused by the polishing process. Similar results were reported earlier in [57] where a rougher surface of bulk GaN was observed after the annealing with pure H₂ at similar temperatures. Mastro *et al.* also performed annealing of HVPE GaN layers with H₂ at different temperatures [58]. It was found that the decomposition of GaN layers started to take place at about 800 °C, via the following reaction: $\text{GaN}^{\text{s}} + 3/4 \text{H}_2^{\text{v}} = \text{Ga}^{\text{l}} + 1/4 \text{N}_2^{\text{v}} + 1/2 \text{NH}_3$.

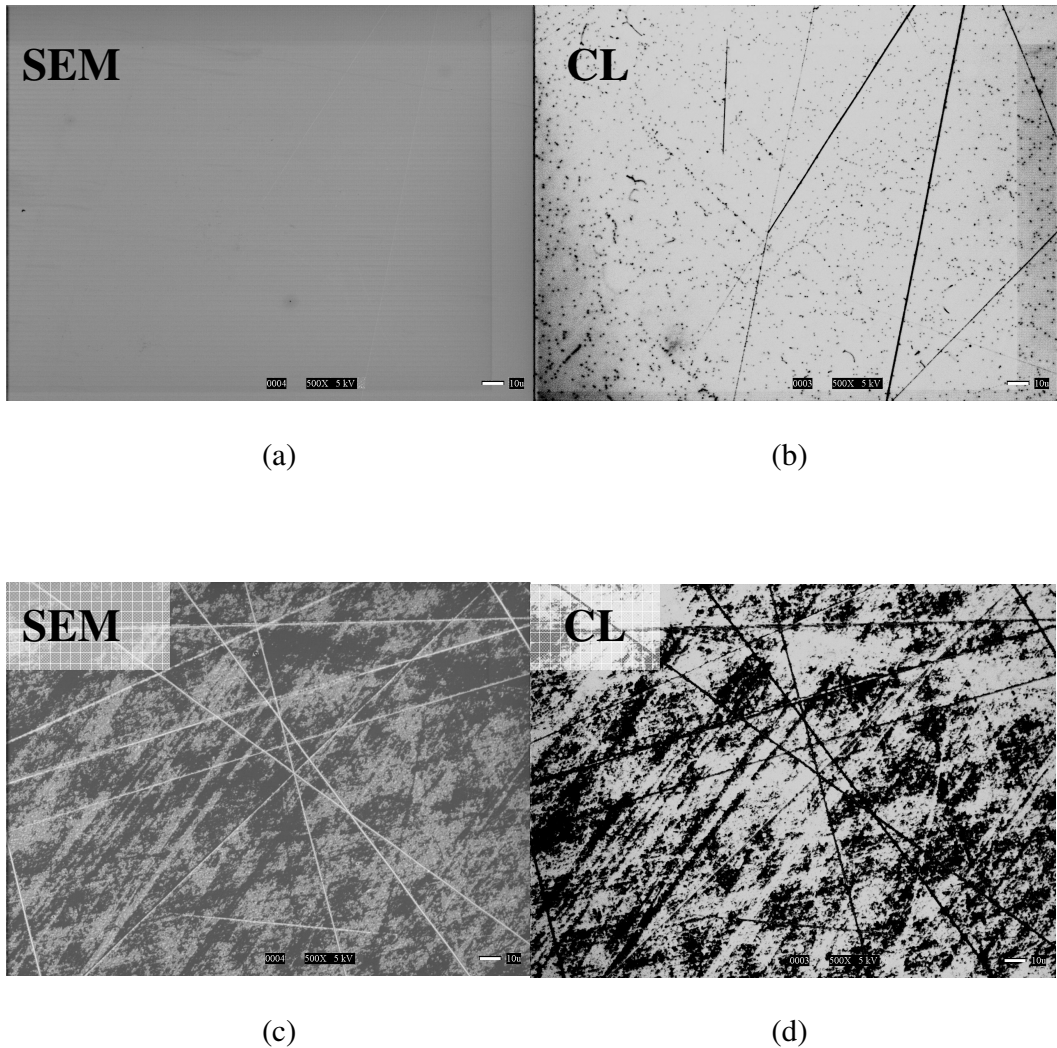


Figure 12. (a) SEM image of Sample A before annealing. (b) Panchromatic CL image taken at the same area, revealing subsurface damages. (c) SEM image of Sample A after the annealing with $\text{NH}_3+\text{H}_2+\text{N}_2$ at $950\text{ }^\circ\text{C}$ for 10 minutes. (d) Panchromatic CL image at the same area. The roughness and scratches were enhanced after annealing and became visible in SEM and CL images. (Image magnification: 500X; scale bar: $10\text{ }\mu\text{m}$; acceleration voltage: 5 kV)

Figures 13 (a) – (d) show the SEM and CL images of Sample B before and after annealing. In Figures 13 (a) and (b), similar features as in Figure 12 (a) and (b) were observed where the SEM image presented a very smooth surface while the CL image revealed the undesired subsurface damages. Figures 13 (c) and (d) present the results after the annealing with NH_3 and N_2 at 950 °C for 60 minutes. As shown in Figure 13 (d), the subsurface damages were significantly reduced after annealing. It should be noted that a thorough search on the annealed surface around the original area was performed with the attempt to locate the same spot in Figure 13 (a) and (b), but it was difficult as most of the scratches in CL images disappeared. The images of Figure 13 (c) and (d) were recorded at the approximate location.

The surface RMS roughness measured by AFM before and after annealing was 0.12 nm and 3.75 nm, respectively. The increase in roughness may be due to a slight surface decomposition during the annealing. Shin et al. reported that GaN crystals showed significant surface roughening after the annealing with pure ammonia at 1130 °C for 2 hours [59]. The surface roughening after ammonia annealing may be due to the reaction between GaN and the H-containing species which were decomposed from NH_3 . It is suspected that Sample B may experience similar effects during the annealing. The result suggested that the etching effect provided by the annealing with NH_3 and N_2 was homogeneous, and able to remove the damaged surface uniformly. Similar observations were reported by Ryu *et al.* where the polish-induced damages in HVPE GaN substrates were found to be recovered after the annealing with pure N_2 [35].

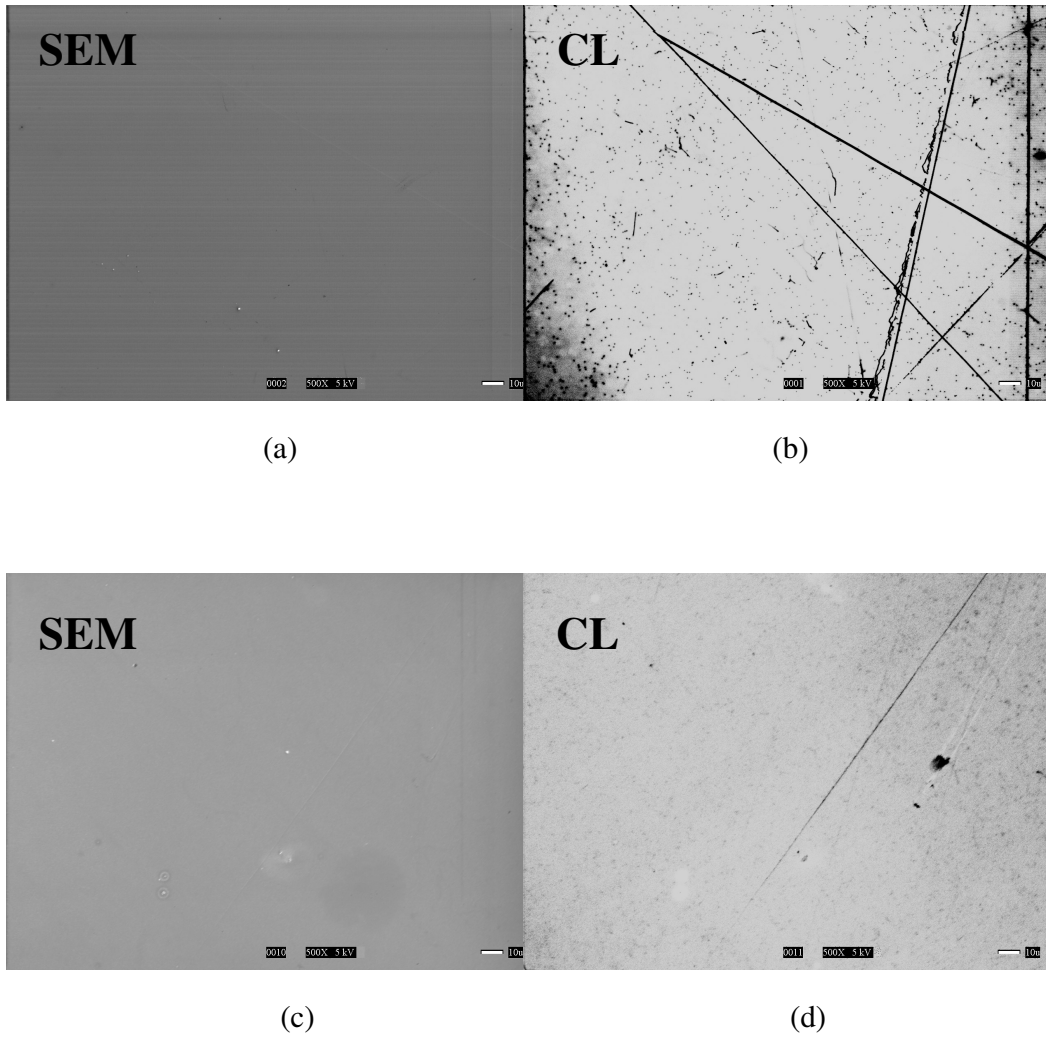


Figure 13. (a) SEM image of Sample B before annealing. (b) Panchromatic CL image at the same area, revealing subsurface damages. (c) SEM image of Sample B after the annealing with NH_3+N_2 at $950\text{ }^\circ\text{C}$ for 60 minutes. (d) Panchromatic CL image at the same area, showing significantly reduced subsurface damages. (Image magnification: 500X; scale bar: $10\text{ }\mu\text{m}$; acceleration voltage: 5 kV)

Figures 14 (a) – (d) show the panchromatic CL images taken at increasing acceleration voltages (5kV, 10kV, 15kV and 20kV) from Sample B after annealing. It was found that the subsurface damage started to become less visible at 15 kV, and almost disappeared at 20 kV. This indicated that the intensity contribution from the damaged subsurface area became less dominant as the electron penetration depth was increased by the higher acceleration voltage. The penetration depth of the electron at 15 kV was estimated to be about 1.48 μm , according to the results by Monte Carlo numerical simulation [37]. It was, therefore, assumed that the damaged area was within the depth of 1.48 μm from the surface.

Figures 15 (a) – (b) show the PL spectra comparison of Sample A and Sample B before and after annealing, respectively. In Figure 15 (a), it can be seen that the near-band-edge emission from Sample A was noticeably reduced after annealing. The reduced near-band-edge emission indicated that surface stoichiometry may be partly destroyed by the H_2 -containing etching gases. The relatively strong (compared to Sample B) yellow luminescence from Sample A may be due to the higher oxygen flows during the HVPE growth [38]. It has been found that oxygen is one of the main sources in GaN leading to the emission around 540 nm [39]. As for Sample B, Figure 15 (b) shows that the PL intensities were comparable before and after annealing. The slightly decreased intensity may be due to a limited surface degeneration during the annealing.

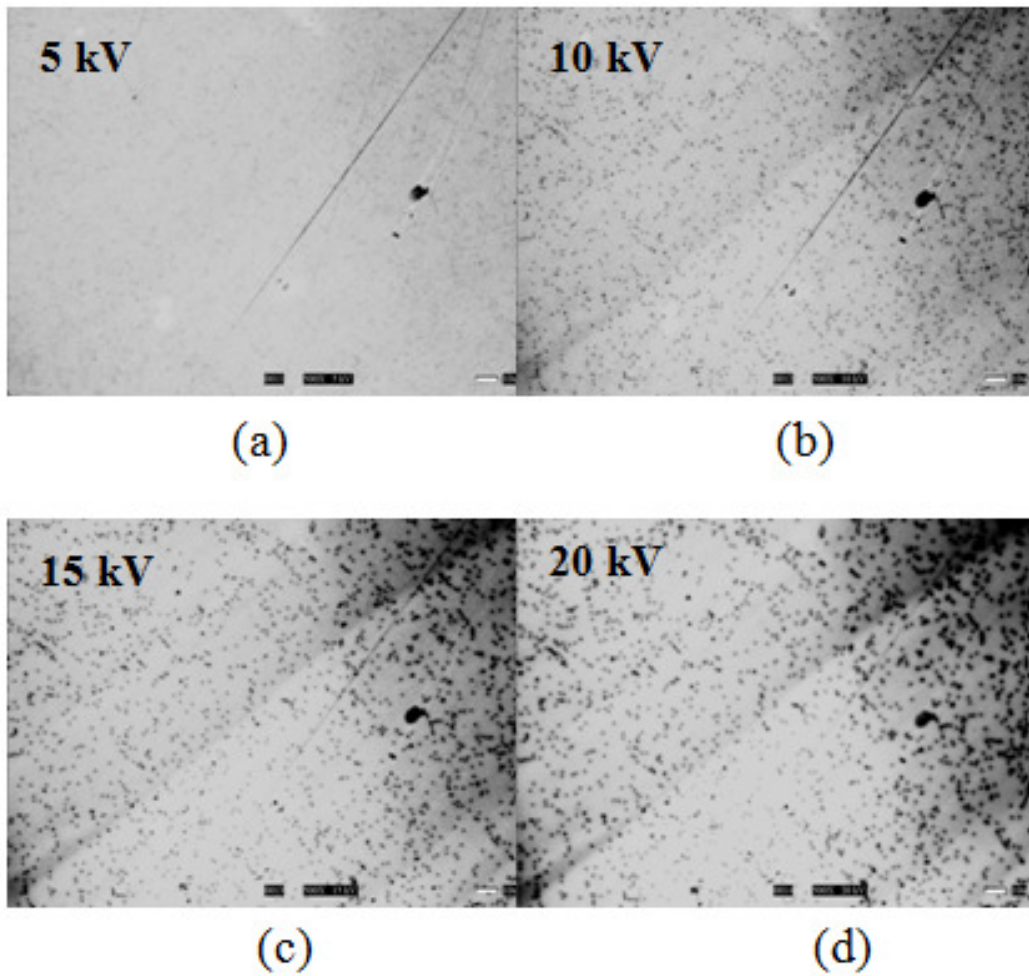


Figure 14. (a) Panchromatic CL images taken from sample at different acceleration voltages: (a) 5 kV, (b) 10 kV, (c) 15 kV, and (d) 20 kV. (Image magnification: 500X; scale bar: 10 μm)

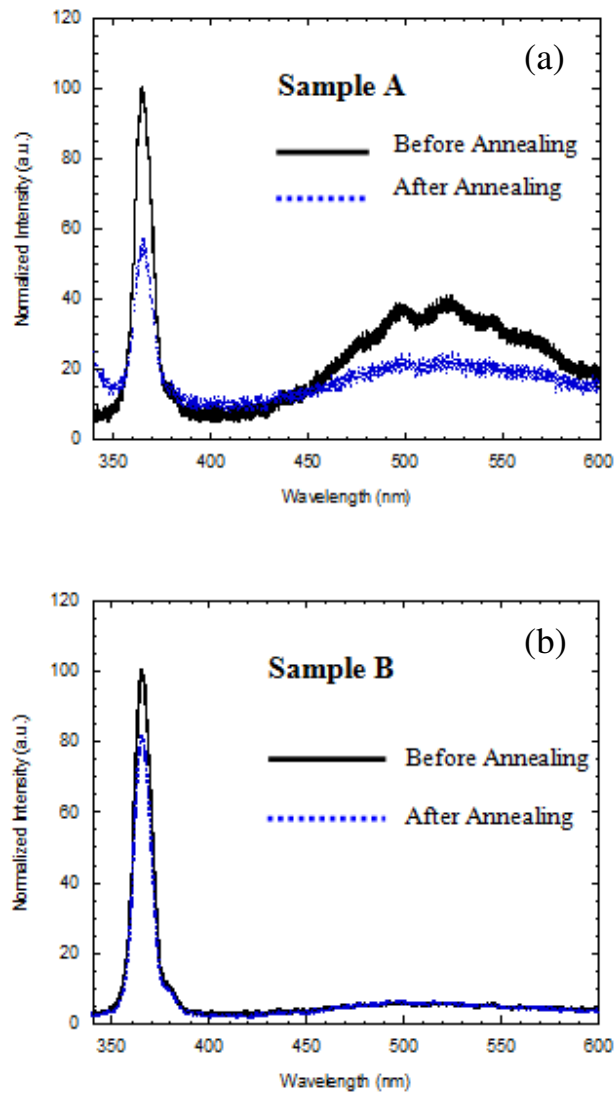


Figure 15. (a) PL spectra of sample A before and after annealing with $\text{NH}_3+\text{H}_2+\text{N}_2$. (b) PL spectra of sample B before and after annealing with NH_3+N_2 .

2.5 Conclusions

M-plane bulk GaN was regrown on m-plane GaN seeds by HVPE. Substantial lateral regrowth was observed in [0001], [11 $\bar{2}$ 0] and [$\bar{1}$ 120] directions. It was found that the regrowth was much faster on (0001) Ga polar surface than that on (0001) N polar surface. The higher growth rate in [0001] was attributed to the thermodynamics in an HVPE system. The 120° angle between the different facets shows the m-plane is one of the preferential expansion planes during the regrowth. The crystal quality of the regrown sample was confirmed by XRD and CL measurements. The dislocation densities in the seed and the regrown areas were approximately $5 \times 10^6 \text{ cm}^{-2}$ and $1 \times 10^6 \text{ cm}^{-2}$, respectively. The high lateral regrowth rate and low dislocation density indicate a feasible method to obtain large-area, high-quality non-polar GaN substrates.

An unoptimized polishing process for GaN substrates could lead to subsurface damages, which were not visible in SEM and AFM, but were revealed in CL images. Thermal annealing was found to be effective in mitigating subsurface damages. However, the annealing with different gas mixtures resulted in substantially different surface morphologies. Annealing with H₂-containing gases at 950 °C led to an inhomogeneous etching effect, and produced a substrate surface with more scratches and enhanced roughness. On the other hand, annealing with NH₃ and N₂ at the same temperature resulted in a substrate surface with noticeably reduced subsurface damages. Surface roughness and optical properties of the sample were slightly sacrificed after the annealing with such gas mixtures. The depth of the subsurface damages was estimated by the CL images taken at different excitation voltages. The results indicated the damaged region was within less than 1.48 μm from the surface.

Since the thermal treatment was carried out in an MOCVD reactor, the annealing conditions with NH_3 and N_2 may be adopted as the preheat step for the homoepitaxial growth of GaN.

CHAPTER 3

Growth of InGaN/GaN Quantum Wells on C-plane

Sapphire

3.1 Introduction

InGaN alloys are the key components to replace conventional light bulbs in the spectrum range from ultraviolet to green. The evaluation of polarization effects on the performance of blue/green LEDs also rely on the successful growth of InGaN-based QWs. It is therefore highly important to establish a repeatable growth condition for the QWs with certain emission wavelength. In this chapter, growth details for InGaN/GaN QWs are provided. Due to the limited number of GaN substrates, the growth was optimized on c-plane sapphire. Methods to determine QWs properties, including peak wavelength and well/barrier thicknesses, are also presented.

3.2 Experimental

InGaN/GaN QWs studied in this project were grown by low pressure (76 torr) MOCVD. Figure 16 shows the layer structure for the QWs. Three periods of InGaN/GaN QWs were grown on 1- μm n-type (carrier concentration: $5 \times 10^{17} \text{ cm}^{-3}$) GaN and capped with 50-nm unintentionally doped GaN. The layers for n_GaN and i_GaN were grown at 1020 °C, and the QWs were grown at 750 °C. Ammonia (NH_3), trimethylgallium (TMGa, for n_GaN and i_GaN), triethylgallium (TEG, for QWs), and trimethylindium (TMIn) were used as the precursors. The carrier gas for TMG and TEG was H_2 and N_2 , respectively. The V/III ratio (ratio of group-V mole fraction to group-III mole fraction) for n_GaN and i_GaN was 3670, while that for well and barrier was 12200 and 33700, respectively.

In order to estimate the thicknesses of well and barrier, high-resolution XRD scans were measured on similar structures. Two samples (Sample 1 and Sample 2) with 10- period QWs were prepared for XRD measurements. The only difference between Samples 1 and 2 was the growth time for well: 20 seconds for Sample 1 and 30 seconds for Sample 2. The layer structures of the two samples followed the one in Figure 16, except the QW periods were ten.

QWs' emissions were revealed by room-temperature PL spectra. The spectra were obtained by 40-mW 325-nm He-Cd laser excitation, with the laser spot size of 1.5 mm in diameter. High-resolution XRD scans were performed with a Cu ($\lambda = 0.154 \text{ nm}$) anode at 27 kV and 20 mA.

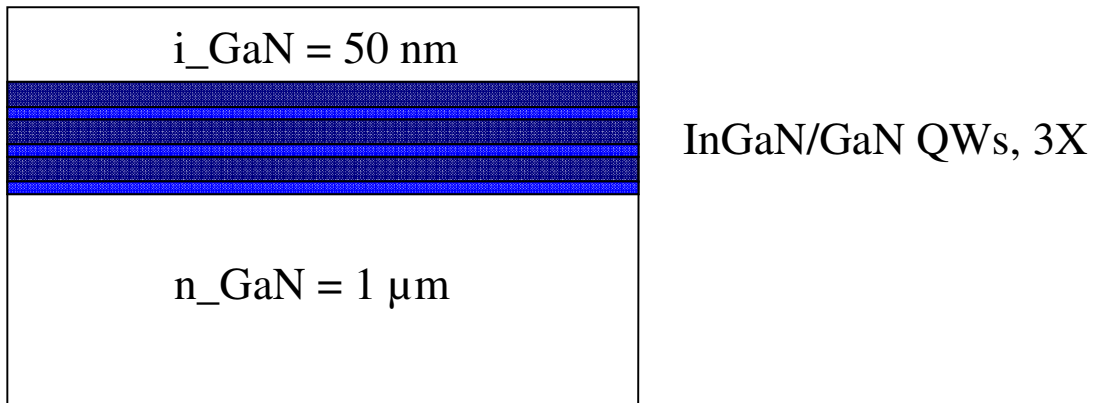


Figure 16. Layer structure of InGaN/GaN QWs.

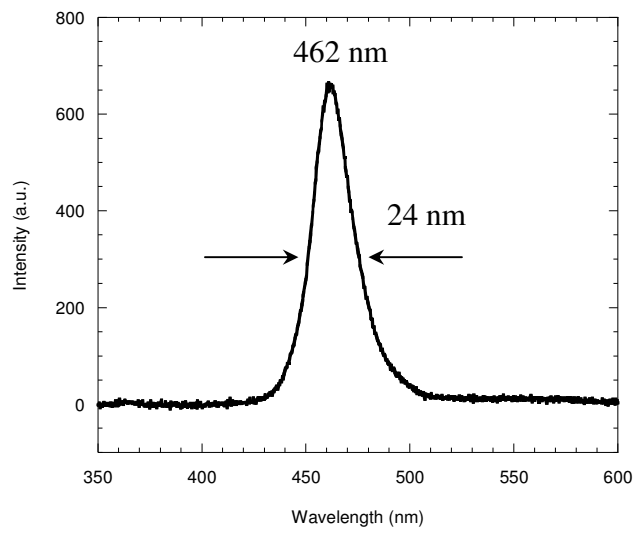


Figure 17. PL spectra from the optimized InGaN/GaN QWs on 2-inch c-plane sapphire.

3.2 Results

Figure 17 presents the PL spectra of the optimized InGaN/GaN OWs. A strong peak at 462 nm was observed. The full width at half maximum (FWHM) was 24 nm

Figure 18 presents the XRD scans on Sample 1 and Sample 2. The main peak is (0002) from the thick n_GaN and the satellite peaks at lower angles are (0002) from the InGaN/GaN superlattice. It can be shown that the distance between satellite peaks relates to the thickness of one period (well plus barrier) [40]. The thickness of a single period can be obtained by Bragg conditions: $2d \sin\theta_n = n\lambda$, where d is the thickness for one period, θ_n is the diffraction angle of the n -th order peak, and λ is the wavelength of x-ray ($\lambda = 0.154$ nm). For Sample 1, the peaks at 16.69° ($n = -1$) and 16.17° ($n = -2$) gave $d_1 = 8.85$ nm. Similarly, the peaks of Sample 2 at 16.68° and 16.25° leads to $d_2 = 10.60$ nm. The difference between d_1 and d_2 ($d_1 - d_2 = 1.75$ nm) should come from the 10-sec growth time difference for the well, indicating the growth rate for well is 0.175 nm/sec. As a result, the well thicknesses for Samples 1 and 2 are 3.50 nm and 5.25 nm, respectively. With well and period thicknesses known, the barrier thickness for the two samples can be obtained: 5.35 nm. The optimized barrier thickness was found to be 6.5 nm.

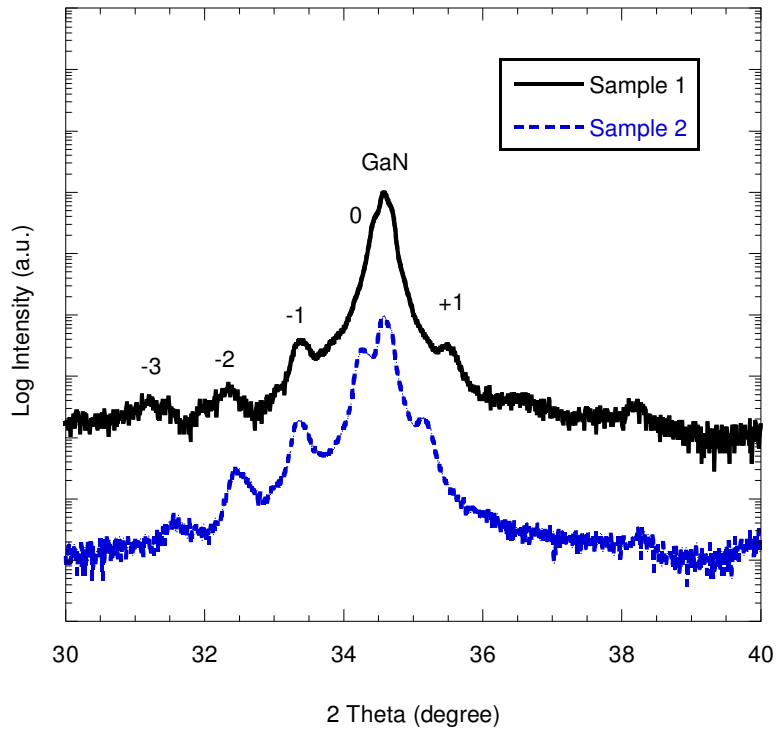


Figure 18. High-resolution XRD scans on Sample 1 and Sample 2.

3.4 Conclusions

InGaN/GaN QWs were grown by MOCVD on c-plane sapphire. PL spectra of the optimized layer structure revealed a strong peak at 462 nm with the FWHM of 24 nm. Well and barrier thicknesses of the QWs were estimated by high-resolution XRD scans. The results indicated that the optimized thicknesses for well and barrier were 3.5 nm and 6.5 nm, respectively.

CHAPTER 4

Effect of Substrate Miscut Angles on Nonpolar InGaN/GaN Quantum Wells

4.1 Introduction

M-plane GaN obtained by slicing from c-plane GaN bulk crystals grown by HVPE is currently among the best substrates for nonpolar nitride-based devices [41]. With defects greatly reduced, m-plane InGaN/GaN LEDs have reached comparable performance to current c-plane LEDs [42].

It was reported that emission intensities and wavelengths from m-plane InGaN/GaN QWs were highly sensitive to the miscut angles of GaN substrates [43]. Although the previous study showed the emission wavelengths from m-plane LEDs was increased by increasing substrate miscut angles toward the $[000\bar{1}]$ (c^- -axis) direction [43], there has been very limited study on the effect of increasing the miscut angles toward the $[11\bar{2}0]$ (a -axis) direction. Furthermore, little work has been done to provide the mechanism explaining the

observations. In this chapter, detailed analysis on the dependence of m-plane InGaN/GaN QWs' properties on GaN substrate misorientation is provided. The goal is to understand how m-plane QW properties, including surface roughness, emission wavelength, and well/barrier interfaces are influenced by the miscut angles of substrates.

4.2 Experimental

Two sets of m-plane GaN substrates were studied. The first set included the substrates containing two different miscut angles toward [0001] c^+ -axis (Sample A: 0.1° ; Sample B: 0.7°); the second set are the substrates with miscut toward a-axis and c^+ -axis (Sample C: 0.1° to a-axis / 0.1° to c^+ -axis; Sample D: 0.1° to a-axis / 0.3° to c^+ -axis). The m-plane substrates were prepared by slicing from c-plane GaN boules grown by HVPE. The exposed m-plane surface was polished mechanically and chemically to obtain high flatness. After the process of surface polish, the miscut angles of the substrates were determined by high-resolution XRD at room temperature using Philips x-ray diffractometer. The diffractometer was equipped with a parabolic graded x-ray mirror collimator followed by a twofold monochromator and a three crystal analyzer.

InGaN/GaN QWs were grown under the same conditions by MOCVD. Before growth, substrate was preheated at 700°C for 10 minutes in the ambient of NH_3 and N_2 , and the temperature was raised to 1020°C for the growth of n-GaN and i-GaN. The QWs were grown at 750°C . Substrate temperature was monitored by infrared pyrometer focused on epitaxial surface. Details of the growth conditions have been described in section 3.2.

Surface roughness of the substrates and the epitaxial films (before and after QW growth) were measured by AFM with the scanning area of $2 \times 2 \mu\text{m}^2$. Before QW growth, AFM was performed on the surface of 0.5- μm n-GaN. After the measurement, the samples were cleaned by boiling solvents, and reloaded in the reactor for subsequent growth. The emissions of the QWs were studied by room temperature cathodoluminescence (CL) with the accelerating voltage of 5 kV and probing current of 0.6 nA.

In compositions and well thicknesses of InGaN/GaN QWs were estimated by secondary ion mass spectrometry (SIMS). SIMS measurement was carried out by a Cameca IMS 6f system. During the measurement, O^{2+} primary ions at the impact energy of 1.25 keV were employed as the sputtering source. The sputtered In ions were detected by their unique mass-to-charge ratio. The incident angle of O^{2+} was 40° from surface normal, and the depth resolution under this condition was about 1.8 and 3.6 nm/decade at the leading and trailing edges, respectively.

4.3 Results

The as-received m-plane GaN substrates exhibited atomic flat surface with RMS roughness in the range of 0.051 – 0.062 nm. Figure 19 shows the AFM image recorded on the substrate surface of Sample D. Smooth morphology with monolayer steps can be seen in the image. Similar surface morphologies were also observed on the substrates of Samples A, B, and C. Figure 20 shows the AFM images of the QWs surfaces on the four samples.

The RMS values measured at different growth steps with the four samples were listed in Table 2. For Samples A and B, with the miscut angles toward a-axis fixed at 0° , it was

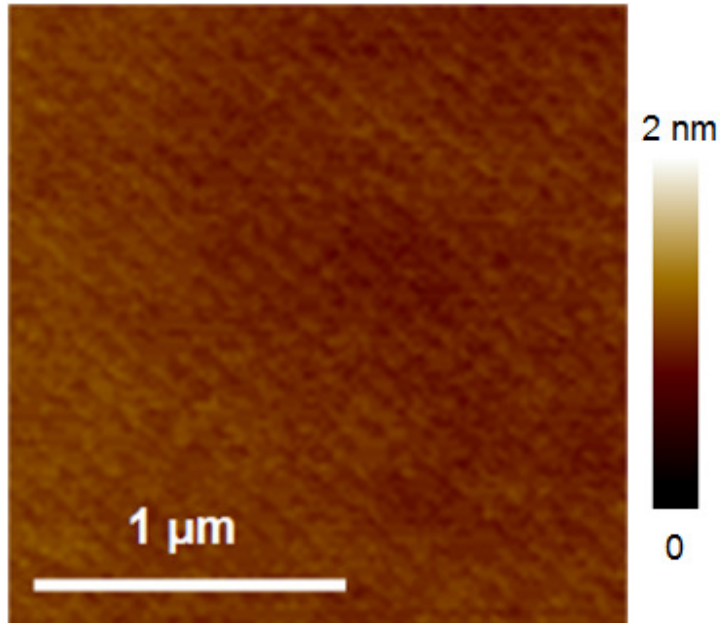


Figure 19. AFM image recorded on the substrate surface of Sample D.

Table 2. Characteristics of Sample A, B, C and D measured by high-resolution XRD, AFM, and CL.

	Miscut Angles a-axis/c-axis	Surface Roughness RMS (nm)			CL Spectra (nm)	
		substrate	n-GaN	QW	peak λ	FWHM
Sample A	0° / 0.1°	0.062	1.39	1.81	411	38.1
Sample B	0° / 0.7°	0.051	3.18	3.97	416	40.7
Sample C	0.1° / 0.1°	0.054	1.28	1.46	404	33.8
Sample D	0.1° / 0.3°	0.056	36.66	47.01	449	57.8

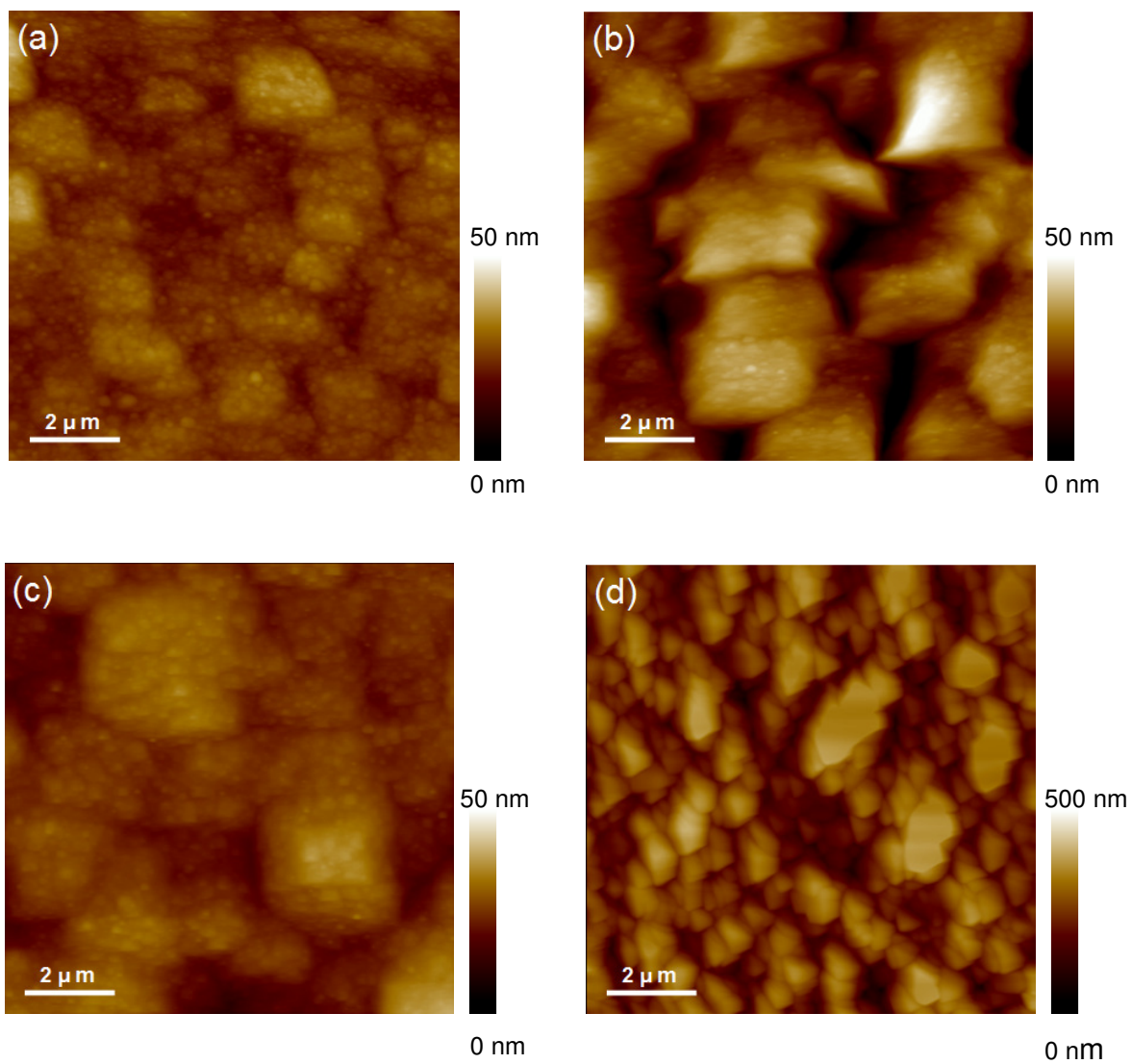


Figure 20. AFM images recorded on the QW surfaces of (a) Sample A, (b) Sample B, (c) Sample C, and (d) Sample D.

found that surface roughness on n-GaN and QWs increased by about 2 times when the miscut was increased from 0.1° to 0.7° toward c^+ -axis. As the miscut toward a-axis increased to 0.1° , which is the case for Samples C and D, the variation of surface roughness was substantially enhanced when the miscut change remained toward c^+ -axis. As shown in Table 2, the RMS values on n-GaN and QWs were increased by more than 25 times when the c^+ -axis miscut was raised from 0.1° to 0.3° . These results indicated that the control range of surface roughness by substrate misorientations can be significantly improved when the miscut angle toward a-axis was slightly increased from 0° to 0.1° .

Figure 21 revealed the CL spectra obtained from the four samples. The peak wavelengths from Samples A and B were 411 nm and 416 nm, respectively. The correlation between surface roughness and emission wavelengths suggested that In incorporation efficiency was increased on rougher surface. It is suspected that the diffusion length of In atoms became shorter when surface roughness was increased. With surface diffusion decreased, the probability of In being incorporated in the InGaN well was improved. The FWHMs for Samples A and B were 38.1 nm and 40.7 nm, respectively. The rougher surface of Sample B may also lead to stronger scattering of In atoms across the well/barrier interfaces, resulting in lower carrier confinement. This can be the reason for Sample B's lower emission intensity and larger FWHM. The difference between Samples C and D became much more evident as the miscut toward a-axis was increased from 0° to 0.1° . With surface roughness significantly enhanced, Sample D produced the peak wavelength of 449 nm, while Sample C only gave the emission at 404 nm. The longer emission wavelength of Sample D was achieved at the sacrifice of intensity and FWHM. Compared with Sample C,

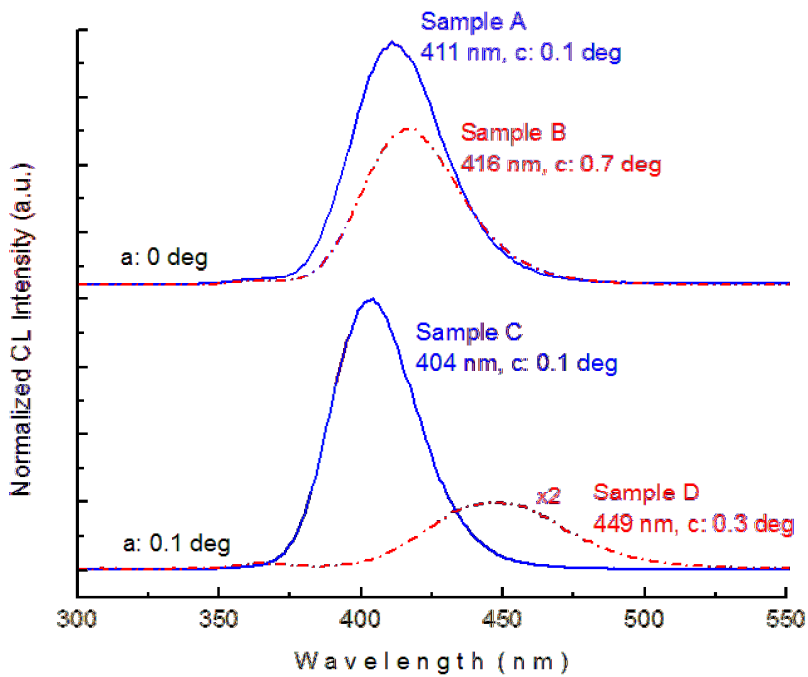


Figure 21. CL spectra measured with Samples A, B, C, and D.

the intensity of Sample D was lower by almost an order, and the FWHM was larger by 1.7 times (57.8 nm vs. 33.8 nm). The degraded emission properties of Sample D were attributed to the stronger atomic scattering as surface roughness increased.

Figure 22 presents In composition depth profiles in the active regions estimated by SIMS with the four samples. Table 3 summarizes the results of SIMS measurements. In Figure 22 (a), the regions of wells and barriers in Samples A and B were defined by the peaks and valleys of the In depth profiles. In compositions in the wells for Samples A and B were respectively 8.6% and 8.8%, showing relatively little difference. However, the difference became larger in the barrier regions, where the compositions for Samples A and B

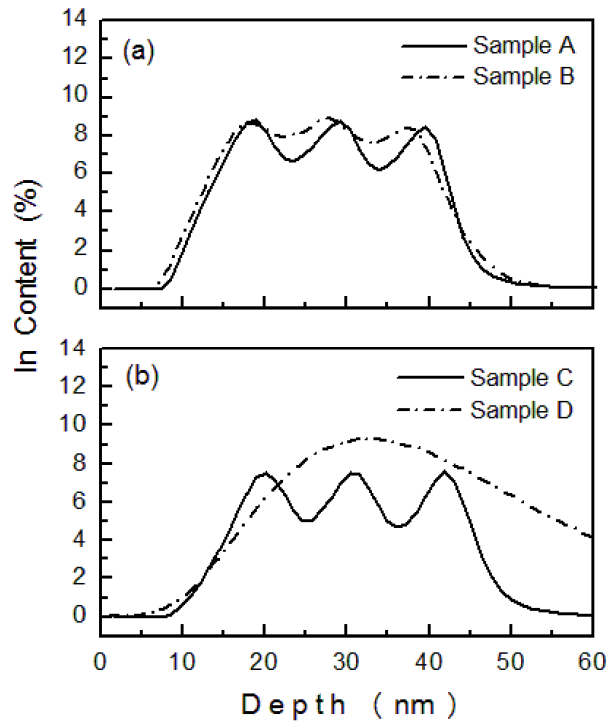


Figure 22. In composition depth profile measured by SIMS for (a) Samples A and B and (b) Samples C and D.

Table 3. Quantum well properties of Sample A, B, C and D estimated by SIMS.

	In compositions (%)		well width (nm)
	well	barrier	
Sample A	8.6	6.5	4.4
Sample B	8.8	7.8	4.0
Sample C	7.5	4.9	4.9
Sample D	9.3	---	---

were 6.5% and 7.8%, respectively. The larger peak-to-valley ratio obtained in Sample A indicated sharper well/barrier interfaces, leading to better carrier confinement. As a result, Sample A produced stronger emission intensities. The well widths were approximated by the averaged FWHMs of the three In peaks. The values thus determined for Samples A and B were 4.4 nm and 4.0 nm, respectively. As the emission wavelength of Sample B is slightly longer than that of Sample A, the narrower well width of Sample B indicated that its longer wavelength was due to the slightly higher In contents in the well regions.

In depth profiles became dramatically different for Samples C and D. As shown in Figure 22 (b), the peak-to-valley ratio in Sample C was even larger those in Samples A and B. This produced the best carrier confinement among the four samples, leading to the highest emission intensity and the smallest FWHM. As for Sample D, the significantly roughened surface achieved the highest In composition of 9.3%. However, the strong surface scattering ruined the well/barrier boundaries, resulting in a merged thick InGaN layer. The emission intensity and FWHM of Sample D were therefore deteriorated.

4.4 Conclusions

The effect of m-plane GaN substrates miscut angles on the properties of InGaN/GaN QWs were investigated. It was found that surface roughness and emission wavelengths of the QWs were highly sensitive to the miscut toward a-axis. With the miscut toward a-axis fixed at 0°, the changes in surface roughness and emission wavelength were less obvious when the miscut toward c-axis increased from 0.1° to 0.7°. As the miscut toward a-axis was increased to 0.1°, surface roughness was enhanced by 25 times and emission wavelength became longer

by 45 nm when the miscut toward c-axis increased from 0.1° to 0.3°. The results indicated that the control range of m-plane QWs' properties can be significantly improved when the substrate miscut toward a-axis was slightly increased from 0° to 0.1°.

CHAPTER 5

Polarization Effects on InGaN/GaN Quantum Wells

5.1 Introduction

In this chapter, the effect of polarization on InGaN/GaN QWs is studied theoretically and experimentally. In theoretical analysis, spontaneous emission rates and emission wavelengths in a single InGaN/GaN QW under different static electrical fields are calculated based on stationary perturbation theory. The purpose is to estimate how much internal field is enough to cause noticeable changes in emission intensities and wavelengths.

In experiments, InGaN/GaN QWs are grown on c-plane and m-plane GaN substrates. There have been numerous reports of LEDs grown on nonpolar GaN substrates [32, 42, 44, 45]. Despite the progress in light output power, two major problems remain to be solved: i) the expected superior light efficiency to that of c-plane LED has not been realized, ii) the emission wavelengths from m-plane (or a-plane) InGaN QWs were found to be significantly shorter than those from c-plane QWs under the same growth condition [45, 46].

Among the reports of LEDs on nonpolar GaN substrates, reduced (relative to c-plane LEDs) or negligible blue-shift with increased drive currents is one of the most common observations leading to the claim that the internal field is eliminated. Most of the reported results provided no data from control samples [32, 42, 44], or employed the QWs grown on c-plane sapphire as the control sample [46]. Since the thermal conductivities of sapphire [47] are at least 5 times lower than those of bulk GaN [48], a lower actual substrate temperature should be expected on sapphire for identically-set growth temperature. This would lead to higher In incorporation efficiency and correspondingly longer emission wavelength. As the atomic diffusion of In is sensitive to temperature [49], the lower actual growth temperature on sapphire may also lead to less In diffusion across the well/barrier interfaces, which is expected to result in difference in emission intensities and wavelengths.

In order to unambiguously demonstrate the effect of polarization, polar and nonpolar InGaN/GaN QWs are respectively grown on c-plane and m-plane GaN substrates. The two types of GaN substrates preserve similar dislocation densities and dimensions.

5.2 Theoretical studies on Quantum-confined Stark Effect

Quantum-confined Stark Effect (QCSE) is the shifting of emission wavelength from a quantum-confined system under the influence of a static electric field [27]. The shifting of wavelength occurs with the changes in emission intensities. The emission intensity from a QW can be estimated by the spontaneous emission rate (SER) in an electron system, which is derived via Fermi's Golden Rule [50]:

$$\mathbf{SER} = \frac{1}{\tau_0} = \frac{q^2 \omega_0^3 |r_{mn}|^2}{3\pi\hbar\epsilon_0 c^3} \quad (5-1)$$

where τ_0 is electron's lifetime, q is the electron charge, ω_0 is the frequency of the perturbing electromagnetic field, $r_{mn} = \langle m|x|n\rangle$ is the dipole matrix element, ϵ_0 is the permittivity in free space, and c is the speed of light. From the equation, it is clearly that SER is proportional to $|r_{mn}|^2$. Assuming the situation that only the first two bound states in the single QW are interactive, r_{mn} can be written as $r_{mn} = \langle 1|x|2\rangle$, where $|1\rangle$ and $|2\rangle$ are the 1st and 2nd bound states in the QW.

Calculating r_{mn} under a constant electric field requires time-independent perturbation theory, where the one-dimensional Schrodinger equation is

$$-\frac{\hbar^2}{2m} \frac{\partial^2}{\partial x^2} |\Psi\rangle + (V + W) |\Psi\rangle = E |\Psi\rangle \quad (5-2)$$

with V the potential distribution of an unperturbed QW, and W the perturbation from a constant electric field. In our case, W is of the form

$$W = -E_0 \left(\frac{x}{L} - 1 \right) \quad (5-3)$$

with L the well thickness, and E_0 the energy change across L . Now the state function $|\Psi\rangle$ is a linear combination of $|1\rangle$ and $|2\rangle$:

$$|\Psi\rangle = A |1\rangle + B |2\rangle \quad (5-4)$$

Plugging (6) into (4) leads to

$$AE_1 |1\rangle + BE_2 |2\rangle + AW |1\rangle + BW |2\rangle = EA |1\rangle + EB |2\rangle \quad (5-5)$$

where E_1 and E_2 are respectively the energy eigenvalues for $|1\rangle$ and $|2\rangle$ of the unperturbed Hamiltonian, and E is the eigenvalue of the perturbed Hamiltonian. Multiplying equation (5-5) by $\langle 1|$, and by $\langle 2|$, and applying the orthonormal properties, equation (5-5) became

$$(E_1 + R - E) A + S B = 0 \quad (5-6a)$$

$$T A + (E_2 + U - E) B = 0 \quad (5-6b)$$

with $R = \langle 1|W|1\rangle$, $S = \langle 1|W|2\rangle$, $T = \langle 2|W|1\rangle$, and $U = \langle 2|W|2\rangle$. In order for the equations to have nontrivial solutions, their determinant must vanish, and solving the resulting expression for E gives

$$E = \frac{1}{2} \{ E_1 + R + E_2 + U \pm [(E_1 + R + E_2 + U)^2 - 4((E_1 + R)(E_2 + U) - ST)]^{1/2} \} \quad (5-7)$$

The values of E_1 and E_2 can be obtained by numerically solving the energy eigenvalues in a single $\text{In}_x\text{Ga}_{1-x}\text{N}/\text{GaN}$ QW. For a QW with finite depth, $|1\rangle$ and $|2\rangle$ are of the form:

$$|1\rangle = C_1 \sin(k_1 x) \quad (5-8a)$$

$$|2\rangle = C_2 \cos(k_2 x) \quad (5-8b)$$

where k_1 and k_2 are the propagation constants, and C_1 and C_2 can be approximated by the normalization integrals

$$\int_{x=0}^L C_1^2 \sin^2(k_1 x) dx = 1 \quad (5-9a)$$

$$\int_{x=0}^L C_2^2 \cos^2(k_2 x) dx = 1 \quad (5-9b)$$

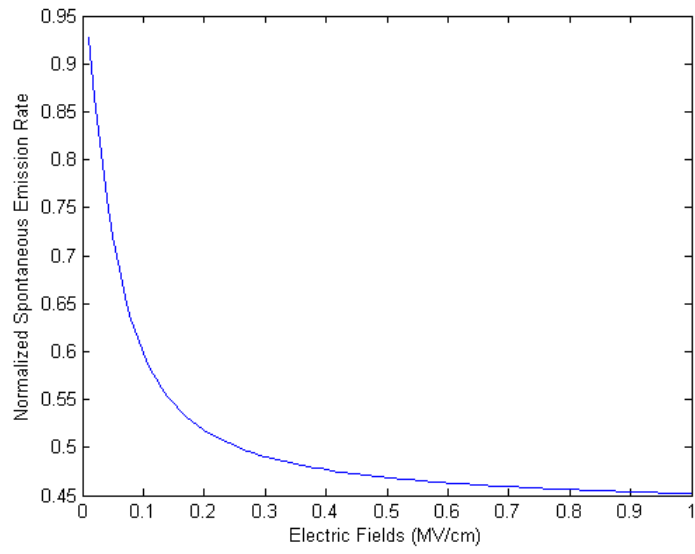
Since the values of the overlap integrals between electron's and hole's wavefunctions outside the QW were less than 1% of the maximum, the evaluation of C_1 and C_2 was

Table 4. Physical parameters used in the calculations for the SER in a single InGaN/GaN quantum well.

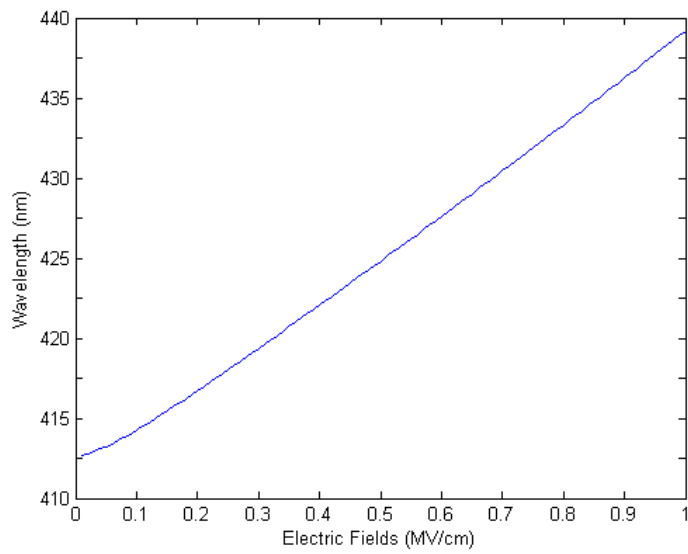
Band gap energy of GaN	3.39 eV [48]
Band gap energy of InN	0.65 eV [49]
Conduction band offset of GaN / InN	0.43 eV [50]
Valence band offset of GaN / InN	1.00 eV [50]
Effective electron / hole masses of GaN	0.20 m_0 / 1.50 m_0 [51]
Effective electron / hole masses of InN	0.11 m_0 / 1.63 m_0 [52]
Well Material	In _{0.15} Ga _{0.85} N
Barrier Material	GaN
Well Width	6 nm

neglected the wavefunctions outside the QW. The perturbed wavefunctions in conduction band and in valence band were obtained by applying electron and heavy-hole effective masses to equation (5-2), respectively. Once electron's and hole's wavefunctions were known, the dipole matrix element r_{mn} can be evaluated. Table 4 lists the physical parameters used in the calculations. All of the parameters for In_xGa_{1-x}N were obtained by applying Vegard's law between GaN and InN.

Figure 23 (a) presents the normalized SER at different magnitudes of electric fields. Evidently, the recombination efficiency fell off as the fields were increased. At the magnitude of 1MV/cm, SER decreased by ~2.2 times. Electric field on the same order of magnitude was predicted by Bernardini *et al.* [23]. The results in Figure 23 (a) were close to the conclusion reported by Takeuchi *et al.* [25], where the crystal orientation dependence of the transition probability in a 3-nm In_{0.1}Ga_{0.9}N/GaN QW was numerically studied. It was



(a)



(b)

Figure 23. (a) The normalized SER at different electric fields in a single $\text{In}_{0.15}\text{Ga}_{0.85}\text{N}/\text{GaN}$ QW. (b) The emission wavelength at different electric fields from the QW.

found that the transition probability became 2.3 times smaller when the electrical field of 0.7 MV/cm was induced by PZ polarization.

Figure 23 (b) gives the emission wavelength from the QW at different electric fields. As the internal electrical field increases, the conduction band and valence band in the QWs become more tilted, causing electrons and holes to stay at the two ends within the well. When electrons and holes are recombined from the tilted bands, a longer wavelength (smaller recombination energy) is expected. In the figure, red-shift up to 25 nm occurred when the fields were increased to 1 MV/cm. The red-shift can be counterbalanced by increased excitation power densities. The process is explained as follows, when more carriers were pumped into QWs at high power densities, the accumulation of electrons and holes produced repulsive Coulomb potential, canceling the force by polarization-induced field. Consequently, electrons and holes were pulled back to each other and flattened the bands, resulting in shorter emission wavelengths. This is one of the reasons that blue-shifts are commonly observed in c-plane QWs when injection currents were increased.

From Figure 23 (a) and (b), correlating the changes in intensities with those in wavelengths leads to the following important observation. At small electrical fields (< 0.2 MV/cm), small change in wavelength can signify big decrease in emission rate. For example, a shift of 4 nm in wavelength (from 412.7 nm at 0.01 MV/cm to 416.7 nm at 0.20 MV/cm) corresponds to the emission-rate decrease of 48 %. On the other hand, for similar wavelength shift at large electrical field (from 433.3 nm at 0.80 MV/cm to 437.4 nm at 0.94 MV/cm), the emission rate only decreases by 0.31 % (for the same change in electrical fields).

5.3 Experimental

InGaN/GaN QWs were grown with identical conditions by MOCVD on m-plane ($1\bar{1}00$) and c-plane (0001) GaN substrates. The same growth conditions were also applied to 1- μm GaN template on c-plane sapphire for comparison. M-plane GaN substrates were obtained by slicing c-plane GaN bulk crystals. Threading dislocations in m-plane and c-plane substrates were evaluated by panchromatic CL images, and they were both in the range of $1\sim 5\times 10^6\text{ cm}^{-2}$. Off-axis angles determined by high-resolution x-ray diffraction (HRXRD) were 0.6° toward [0001] for m-plane GaN, and 0.6° toward [$1\bar{1}00$] for c-plane GaN. The dimensions for m-plane and c-plane substrates were $10\times 3\text{ mm}^3$ and $10\times 4\text{ mm}^3$, respectively. The dimension for GaN template on sapphire was 2 inch in diameter.

Details of the QWs growth are described in sections 3.2 and 4.2. Indium compositions in the active regions were estimated by high-resolution XRD and SIMS, and they were 5.3%, 5.4%, and 8.7% for the QWs on m-plane GaN (m-GaN), c-plane GaN (c-GaN) and c-plane sapphire (c-sapphire), respectively. Optical properties of the QWs were investigated by room-temperature CL spectra with the wavelength resolution of 0.5 nm. During the measurements, electron beams with the acceleration voltage of 5 kV were injected to the scanning area of $10\times 6\text{ }\mu\text{m}^2$, and the probe currents varied from 0.1 nA to 1000 nA, corresponding to the current densities from $1.67\times 10^{-4}\text{ A/cm}^2$ to 1.67 A/cm^2 . In order to determine the well thicknesses, cross-sectional TEM images were recorded on the active regions. TEM samples were prepared by focus ion beam (FIB) using Ga ion at 30 kV.

5.4 Results

Figure 24 shows CL spectra taken from the QWs grown on these substrates. One can see that the peak emissions of the three samples appeared at 397.0 nm (m-GaN), 416.5 nm (c-GaN), and 458.5 nm (c-sapphire). Despite the same growth condition, the wavelength observed on c-sapphire was longer than that on c-GaN. This may be attributed to the lower thermal conductivity of sapphire. Although the susceptor temperatures were set to be identical, the lower thermal conductivity of sapphire resulted in poorer coupling of the substrate to the susceptor. This led to a lower actual growth temperature, and correspondingly higher In incorporation efficiency.

Comparing the emissions from QWs grown homoepitaxially on m-GaN and c-GaN, it can be seen that the intensity of m-plane QWs was about 2 times stronger than that of c-plane QWs. The intensity difference between m-plane and c-plane QWs was very close to the theoretical results in section 5.2 and the ones reported by Takeuchi *et al.* [25]. The peak wavelengths for m-plane and c-plane QWs were 397.0 nm and 416.5 nm, respectively. The value of wavelength difference is less than the ones reported by other researchers, where the peaks were 402 nm for m-plane QWs and 450-460 nm for c-plane QWs [46]. It was noticed that the peaks of c-plane QWs in Ref. [46] were obtained on c-plane sapphire. As the thermal conductivity of sapphire is lower than that of GaN [47,48], the larger discrepancy may result from the difference in real growth temperature between sapphire and GaN substrates. In Figure 24, since comparable experimental conditions were applied to m-plane and c-plane QWs, the longer peak wavelength of c-plane QWs was believed to result from the tilted

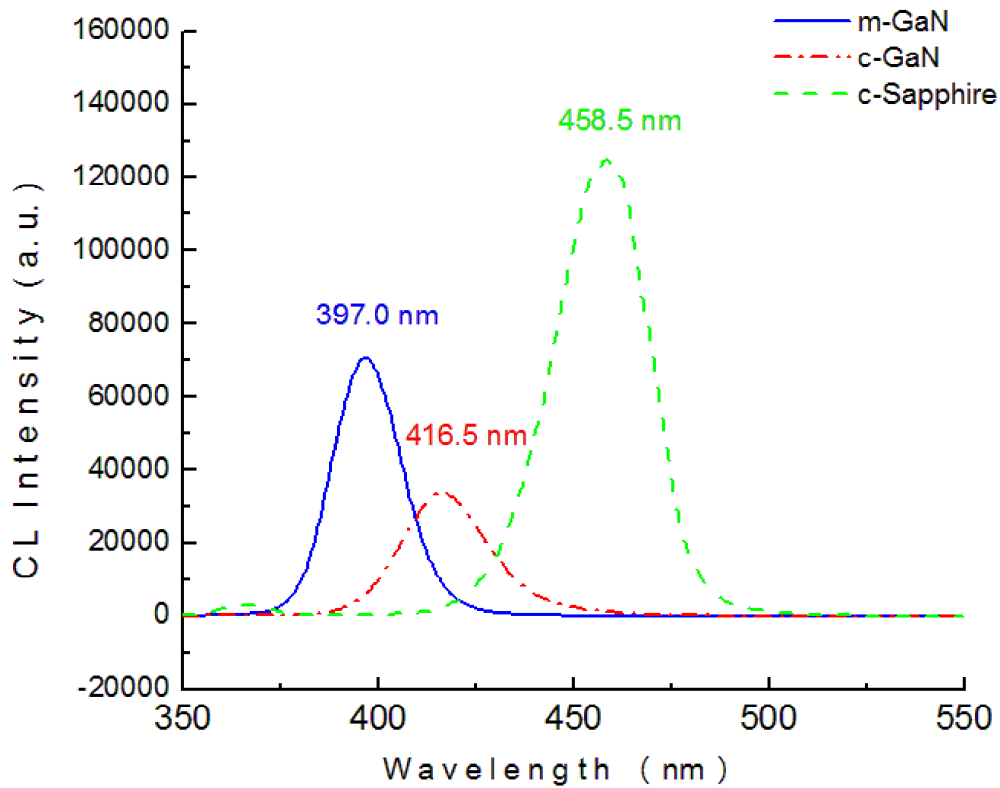


Figure 24. CL spectra taken from the QWs grown m-plane GaN, c-plane GaN and c-plane Sapphire. Probe current: 10 nA.

bands caused by QCSE. The FWHMs for m-plane and c-plane QWs were 20.0 nm and 24.5 nm, respectively. It is suspected that the slightly larger FWHM of c-plane QWs was caused by the additional contributions of the sub-bands formed in the tilted QWs.

Figure 25 present the cross-sectional TEM images at the active regions of the three samples. The image of the m-plane structure was taken at the [0001] zone axis, while the c-plane images were taken at the [1100] zone. It was found that the QW boundaries were

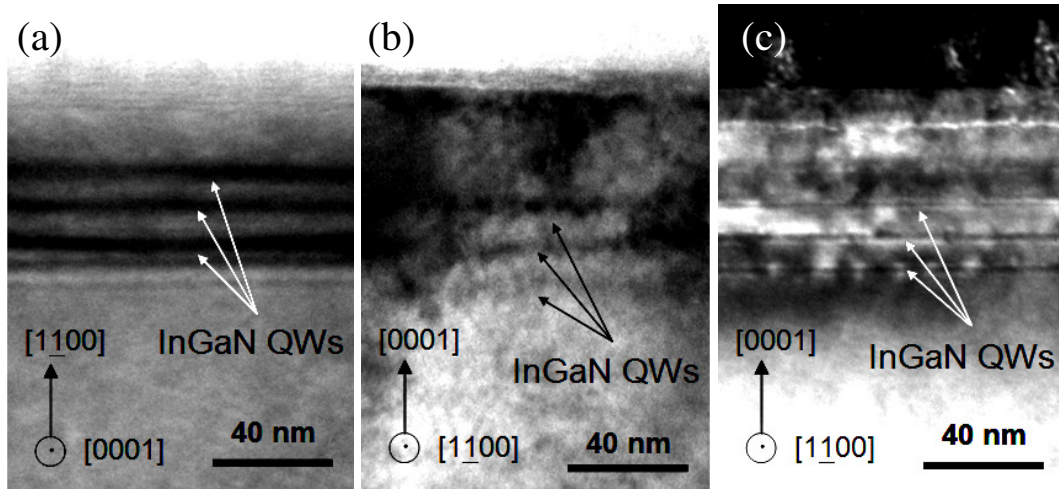


Figure 25. Cross-sectional TEM images taken in the InGaN/GaN QWs grown on: (a) m-plane GaN, (b) c-plane GaN, and (c) c-plane sapphire.

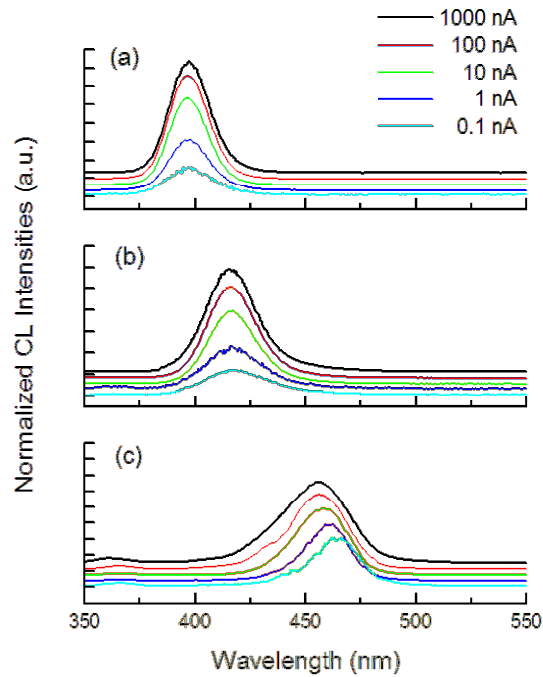


Figure 26. Normalized CL spectra at different probe currents measured with the QWs grown on: (a) m-plane GaN, (b) c-plane GaN, and (c) c-plane sapphire.

sharper on sapphire than on GaN substrates. The sharper QW interfaces on sapphire indicated better carrier confinement, and this explained the strongest emission intensities seen in Figure 24. The less-sharp boundaries and larger well widths on GaN substrates were possibly due to the stronger diffusion of In atoms across well/barrier interfaces [49]. Since the actual growth temperature on GaN should be higher due to its higher thermal conductivity, stronger In diffusion was expected in the QWs grown on GaN substrates. The QW width in the structures grown on m-GaN and c-GaN were found to be about 4.5 nm, while the one on c-sapphire were 2.0 nm. The thinner well widths and longer emission wavelength of the QWs on c-sapphire indicated a higher In incorporation efficiency, and this was in correspondence with In compositions estimated by SIMS and XRD.

Figure 26 shows normalized CL spectra from the three samples at different probe currents. Clear blue-shift was observed on c-sapphire. In Figure 22 (c), the peak wavelength on sapphire shifted from 465.0 nm at 0.1 nA to 456.0 nm at 1000 nA. The blue-shift can be explained by the combined effects of band filling and screening of QCSE. In band filling, as the carrier densities in QWs were increased with higher driving currents, electrons and holes can fill up to higher energy states and be recombined from there. Blue-shift therefore occurred. In the screening of QCSE, when more carriers were pumped into QWs, the accumulation of electrons and holes produced repulsive Coulomb potential, counterbalancing the force by polarization-induced field. Consequently, electrons and holes were pulled back to each other and flattened the bands of QWs, resulting in larger recombination energies.

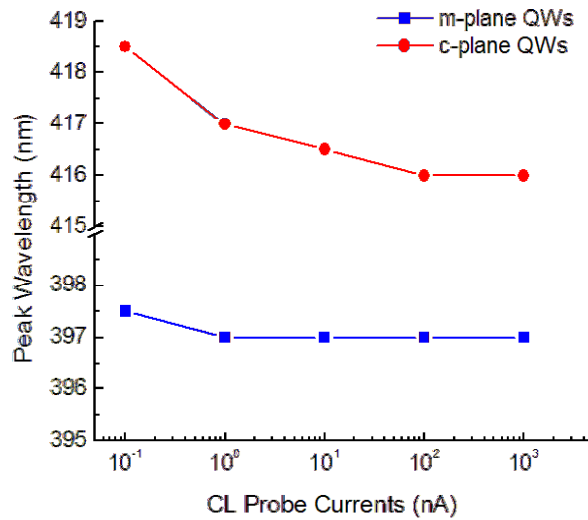


Figure 27. CL Peak wavelengths at different probe currents for QWs on c-GaN and m-GaN.

As the wavelength shifts in Figure 26 (a) and (b) were less apparent, peak wavelengths as a function of probe currents were plotted for c-GaN and m-GaN in Figure 27. In the figure, the peak shifted from 418.5 nm at 0.1 nA to 416.0 nm at 1000 nA for c-plane QWs, whereas very limited shifts were observed on m-plane QWs. It should be noted that the blue-shift may result from different mechanisms, such as band filling and screening of QCSE. However, since comparable experimental conditions were applied to m-plane and c-plane QWs, the larger blue-shift produced by c-plane QWs clearly demonstrated that the polarization effect existed, and was screened when the current densities in the QWs increased at larger probe currents.

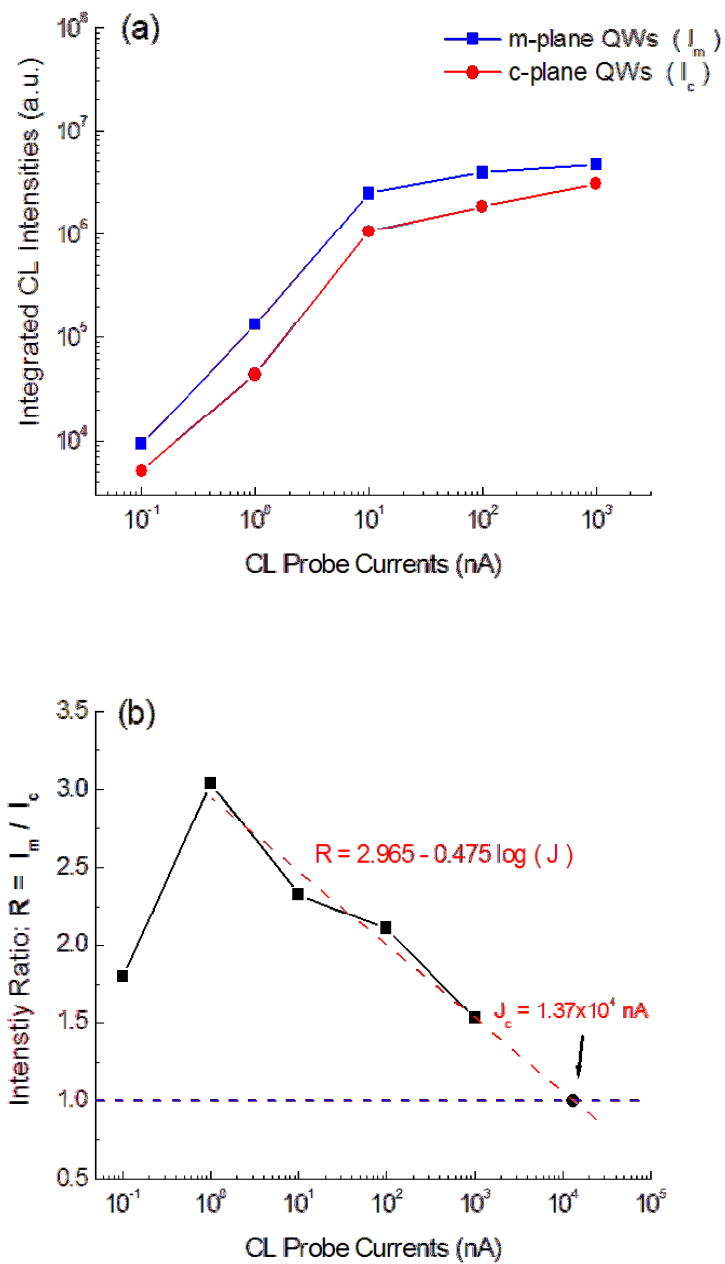


Figure 28. (a) The integrated CL emission intensities of the QWs on m-GaN and c-GaN at different CL probe currents. (b) The integrated CL intensity ratios of the QWs on m-GaN and c-GaN, defined as $R = I_m / I_c$, at different CL probe currents.

Figure 28 (a) exhibits the integrated CL intensities of the QWs grown on c-GaN and m-GaN. From the figure, it can be seen that the slopes of the two lines for c-plane and m-plane QWs decreased after the probe currents reached 10 nA. The efficiency drop is also observed by other groups [32, 51], and possible causes included Auger recombination in InGaN [52] and current leakage through the QWs [53].

An important observation in Figure 28 (a) is that the intensity difference between m-plane and c-plane QWs gradually decreased as the probe currents increased from 1 nA to 1000 nA. The trend is more obvious when the integrated intensity ratio R was plotted as a function of probe currents, shown in Figure 28 (b). The intensity ratio R was defined as $R = I_m / I_c$ where I_m and I_c are the integrated CL intensities for m-plane QWs and c-plane QWs, respectively. Except the case at 0.1 nA, where the band filling of localized energy states in QWs may dominate, the ratio decreased from 3.04 at 1 nA to 1.53 at 1000 nA. This observation can be explained by the schematic shown in Figure 29. At low probe current (1 nA), the carriers within c-plane QWs provided relatively small Coulomb potential to counterbalance the polarization-induced electrical field, leading to stronger band tilting. For m-plane QWs, if no internal field was assumed, the bands were flat. This implies a larger difference in recombination efficiency between m-plane and c-plane QWs. When the probe current became higher (> 1 nA), since more carriers were pumped into the QWs, the increased Coulomb potential produced stronger repulsive field to cancel the polarization-induced field in c-plane QWs. The bands in c-plane QWs then became less tilted, and therefore the efficiency drops in c-plane QWs were mitigated at high probe currents. Since no internal field was assumed in m-plane QWs, the bands remained flat at high probe

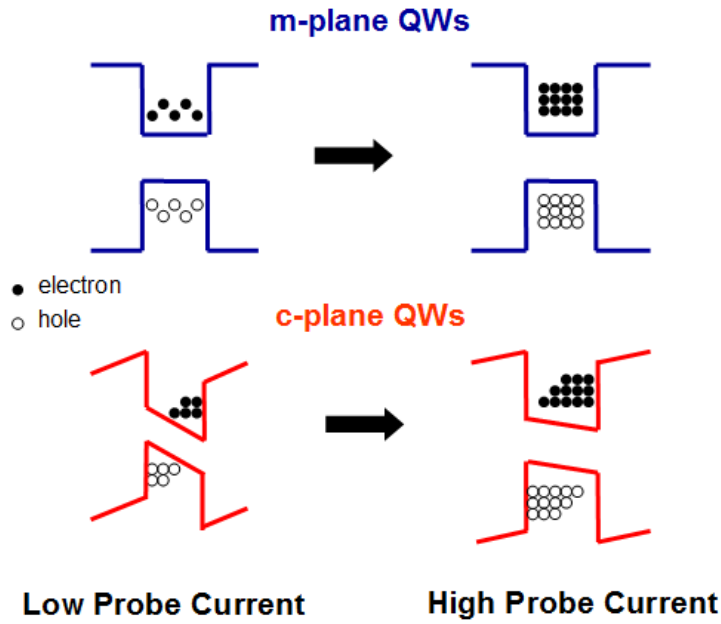


Figure 29. Schematic illustration of m-plane and c-plane QWs at low and high probe currents.

currents. As a result, the difference in recombination efficiency between the two types of QW decreased at high probe currents.

As the probe current of 1000 nA reached the upper limit of the CL system, logarithmic fitting was applied in Figure 28 (b) for the points at 1 nA ~ 1000 nA. The fitting was performed with the attempt to find the critical current where the integrated intensity of c-plane QWs equaled that of m-plane QWs, i.e. $R = 1$. The relationship between the intensity ratio R and the probe current J (in nA) approximately followed the equation:

$$R = 2.965 - 0.475 \log (J) \quad (5-10)$$

It was found that $J_c = 1.37 \times 10^4$ nA for $R = 1$. The value of J_c corresponds to the current density of 22.84 A/cm^2 . This means that when $J = J_c$, the number of carriers pumped into c-

plane QWs was enough to produce the electrical field with the same magnitude but the opposite direction as the field induced by piezoelectric and spontaneous polarizations. As the value of J_c depends on carrier concentrations and polarizations experienced by the QWs, different J_c 's should be expected for the QWs with different well thicknesses and In compositions.

5.5 Conclusions

Theoretical treatments based on stationary perturbation theory were performed to evaluate QCSE in a single InGaN/GaN QW. The results showed that spontaneous emission rate dropped by 220 % and peak wavelength increased by 25 nm when the internal electrical field increased from 0 to 1 MV/cm.

InGaN/GaN QWs were grown on m-plane and c-plane GaN substrates with similar experimental conditions. Higher emission intensities and shorter peak wavelengths were obtained on m-plane QWs. These were attributed to the reduced or eliminated QCSE in m-plane QWs. As CL probe current increased from 0.1 nA to 1000 nA, blue-shift of 2.5 nm was observed in c-plane QWs, while very limited wavelength shift was seen in m-plane QWs. The intensity ratio of m-plane QWs to c-plane QWs was found to decrease as the probe current increased. The trend can be explained by the screening of QCSE in c-plane QWs, and approximately followed the equation: $R = 2.965 - 0.475 \log (J)$.

CHAPTER 6

The Emissions of Nonpolar InGaN/GaN Quantum Wells under Biases

6.1 Introduction

When the dependence of internal fields on crystal orientation was theoretically evaluated, two dimensional ideal QWs were assumed in the InGaN active regions [25]. However, as described in section 1.2, there is a tendency in InGaN towards quantum-dot (QD)-like structures due to the phase separation of InN and GaN.

If the 3-dimensional carrier confinement (QD) is formed in the active region, a finite electrical field in the lateral direction (perpendicular to the growth direction) should be considered. This is due to the fact that even the QWs are grown along the nonpolar directions (either $[1\bar{1}00]$ or $[11\bar{2}0]$), the strong SP and PZ polarizations still stay along the c-axis $[0001]$ [54]. Since material discontinuity along the lateral $\langle 0001 \rangle$ direction exists in the QD-like structure, finite electrical field should be induced by SP and PZ polarization along the

<0001> direction [23]. As shown in section 1.4, the relation between electrical field and polarization is governed by the equation:

$$\mathbf{D} = \epsilon\mathbf{E} + \mathbf{P} \quad (6-1)$$

with \mathbf{D} the displacement field, \mathbf{E} the electrical field, \mathbf{P} the macroscopic polarization, and ϵ the static dielectric constant. The displacement field \mathbf{D} is determined by the free-charge distribution in the material:

$$\nabla \cdot \mathbf{D} = e(p - n) \quad (6-2)$$

with e the electron charge, and p and n the hole and electron concentrations, respectively.

When carriers are excited in the QDs, equal number of electrons and holes can be assumed, which implies the charge neutrality, i.e., $\nabla \cdot \mathbf{D} = e(p - n) = 0$. For the QWs grown along the nonpolar directions, since $\mathbf{D} = 0$ and $\mathbf{P} \neq 0$ along <0001>, equation (6-1) tells that $\mathbf{E} \neq 0$ in <0001>. Such finite electrical field will still laterally pull electrons and holes apart within the QDs, and adversely affect the radiative recombination efficiency. In other words, wavelength shifts under the influence of static electric field due to QCSE should still be preserved in nonpolar LEDs.

An intuitive approach to investigate the possible QCSE in nonpolar QWs is to apply an external field along <0001>, and observe how the QWs' emission changes with the external field. A similar measurement has been performed on a single InGaN layer grown on c-plane sapphire, and red-shift of more than 5 meV was observed by micro-PL under the lateral bias of 10V [55]. The results indicated that carriers are confined 3-dimensionally in the active region. Therefore, when the lateral electrical field was applied, electrons and holes were pulled away from each other in the tilted bands, and resulted in lower recombination

energies (red-shift). Similar measurement performed on the QWs grown on nonpolar GaN substrates would provide the direct evidence for the lateral polarization-induced fields.

In this chapter, lateral biases are externally applied to m-plane InGaN/GaN QWs during microPL measurements. The purpose is to investigate the possible internal electrical field induced by the polarizations exerting on the dot-like structures in the InGaN layers.

6.2 Experimental

InGaN/GaN QWs were grown by MOCVD on m-plane GaN substrates. The miscut angle of the substrate was 0.6° toward $[0001] c^+$ -axis. The growth conditions were described in sections 3.2 and 4.2.

In order to apply DC bias across the QWs, square metal contacts were fabricated on the epitaxial surface with standard lithography. Negative photo-resist AZ5214 was applied to pattern the film surface. After the lithography, Ti (30nm)/Al (90nm) were deposited on the sample by e-beam evaporator to form ohmic contact. The dimensions of the contacts were $300 \times 300 \mu\text{m}^2$, and gaps between adjacent contacts were $1.2 \mu\text{m}$.

The QWs' emissions under biases were measured by a microPL system with the spot size of $5 \mu\text{m}$ in diameter. Optical signals were excited by 325 nm He-Cd laser with the power of 200-mW. During the measurements, DC biases from 0V to 30V were applied across the gaps of adjacent ohmic contacts in order to induce changes in wavelengths and intensities. The measurement was carried out at Auburn University, Alabama. Figure 30 shows the schematic of the measurement set-up.

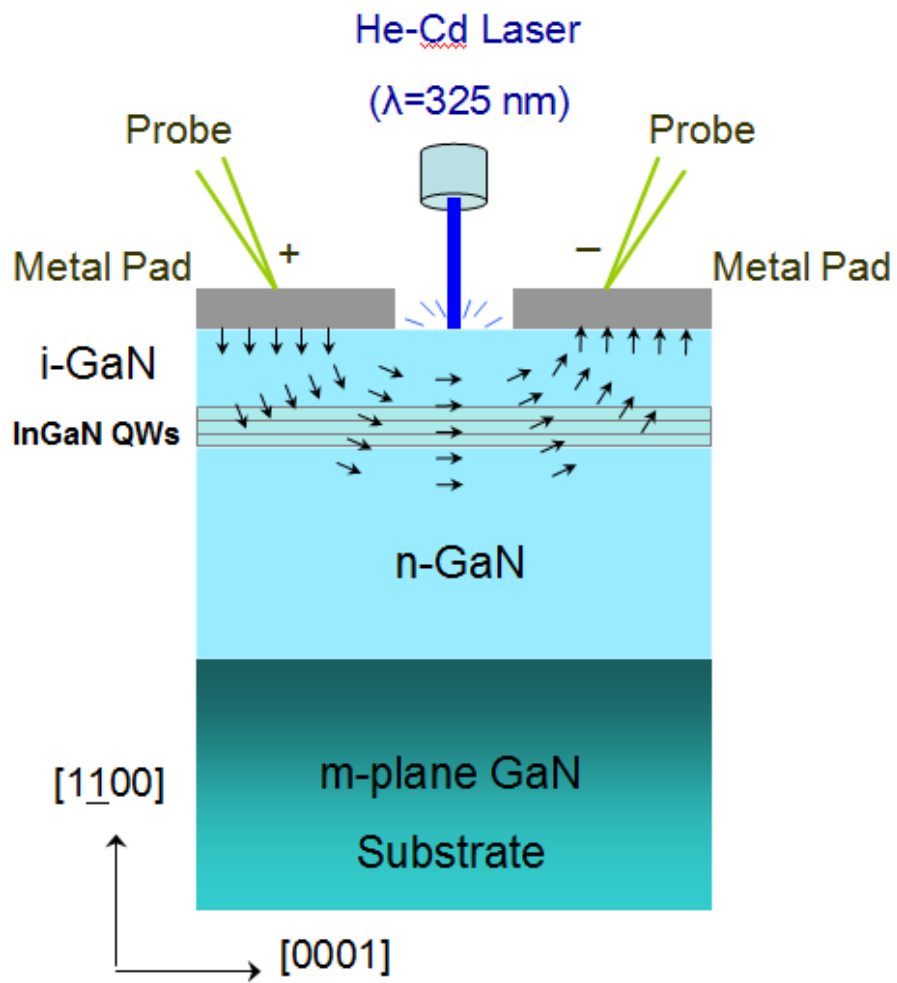


Figure 30. Schematic illustration of biased microPL measurement set-up.

6.3 Results

The first attempt of measurement was not successful. It was found that the laser spot size of the micro-PL system was too large to excite any signal from the 1.2- μm gap. Measurable optical signals from the QWs could only be obtained at the edge, where 1/3 of the laser beam spot covered the gap area, and the rest beam spot covered the bare area (no metal pads). Figure 31 gives the schematic showing the relevant positions of beam spot. It was reported that the polarization-induced field in wurtzite GaN was along $[000\bar{1}]$ [56]. The first external bias was therefore chosen to be along the opposite direction, i.e., $[0001]$ in order counterbalance the existing field. After the laser beam was focused at the gap edge, DC bias up to 30 V was applied during the spectra measurement.

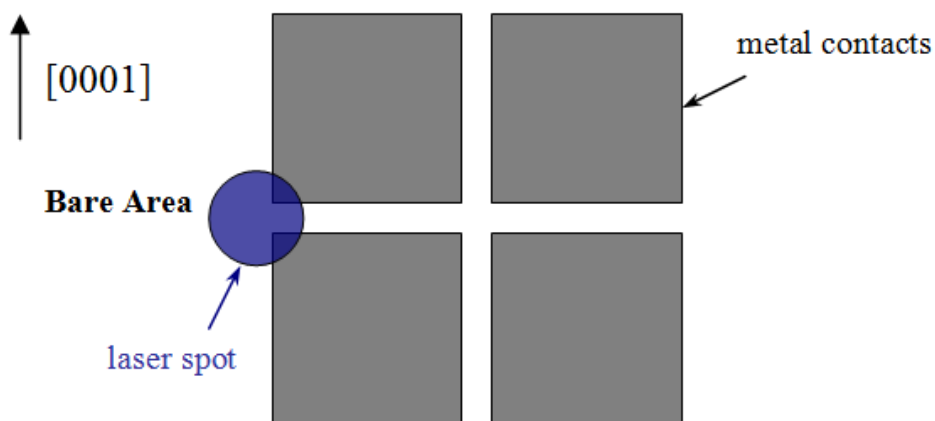


Figure 31. Schematic showing the relevant position of laser beam spot on the surface of m-plane QWs. Dimensions are not to scale.

Figure 32 presents the micro-PL spectra from the m-plane InGaN/GaN QWs under different biases. Both forward (+ 30V, along [0001]) and reverse (- 30V, along [000 $\bar{1}$]) biases were applied during the measurement. The spectra showed negligible change under either bias. The results indicated the applied biases were not high enough to cause any change in the QWs' emission.

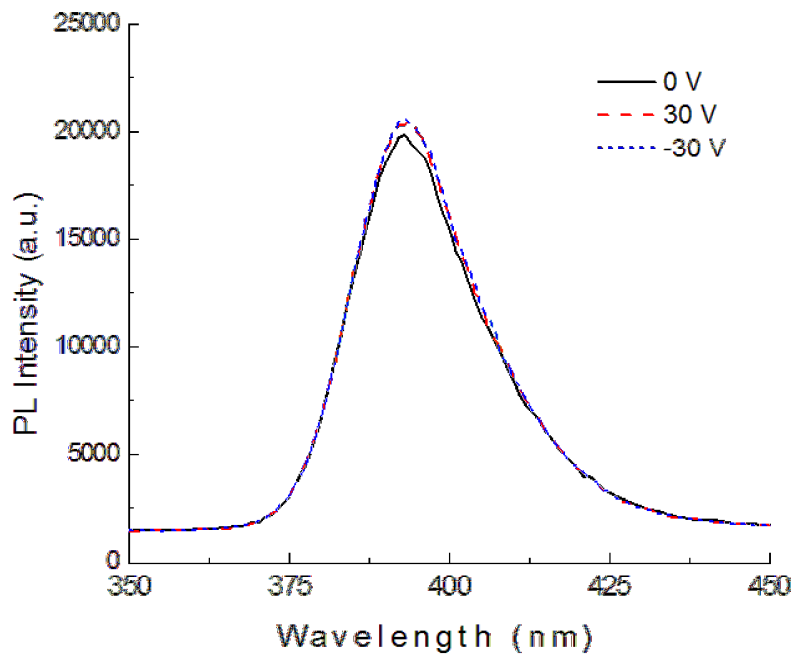


Figure 32. Micro-PL spectra from m-plane InGaN/GaN QWs under different DC biases

In order to estimate the lateral fields generated by the applied biases, a commercial simulation package (ATLAS, Silvaco International) was used to calculate the static field distribution within the 1.2- μm gap. During the simulation, the thin InGaN well layers were neglected, and carrier concentration for i_GaN was assumed to be $5 \times 10^{16} \text{ cm}^{-3}$.

Figure 33 gives simulation results under 30V. Most of the gap area was under the field of 0.34 MV/cm, and the maximum of 1.70 MV/cm occurred at the contact end. It should be noted that the calculations were performed in an ideal gap area. In the case of Figure 31, the electric field at the gap edge, where the optical signals were collected, should be much less than the simulated values.

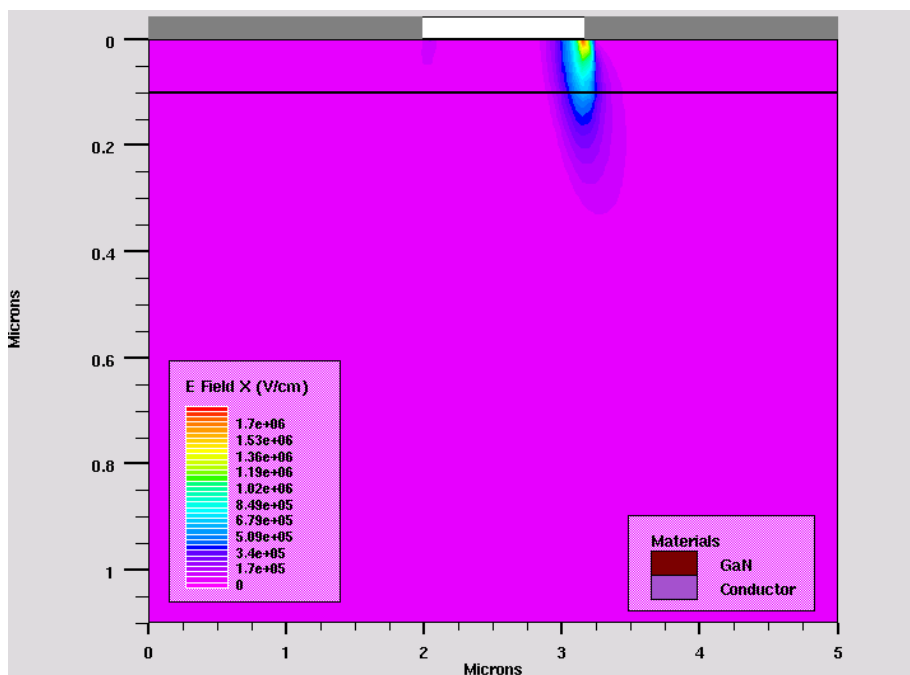


Figure 33. Simulated lateral electric field distribution within the 1.2 μm gap of adjacent contacts under a DC bias of 30 V

Robinson *et al.* carried out similar measurement on a single InGaN layer grown on c-plane sapphire [55]. Figure 34 shows the results of microPL measurements in Ref. [55]. In the figure, a red-shift of $\Delta E = -5.4$ meV was observed at the bias of 10 V. The results indicated that electrons and holes were pulled apart in the dot-like structures as lateral bias increased. In m-plane QWs, if similar dot-like structures exist, the lateral bias is expected to result in blue-shift (i.e., $\Delta E > 0$). This is because the carriers should be separated in the dot structure at 0 bias by the polarization-induced field, which is along c-axis. The separation of carriers should decrease if the bias is increased to counterbalance the existing field, leading to the flat band condition and larger recombination energies.

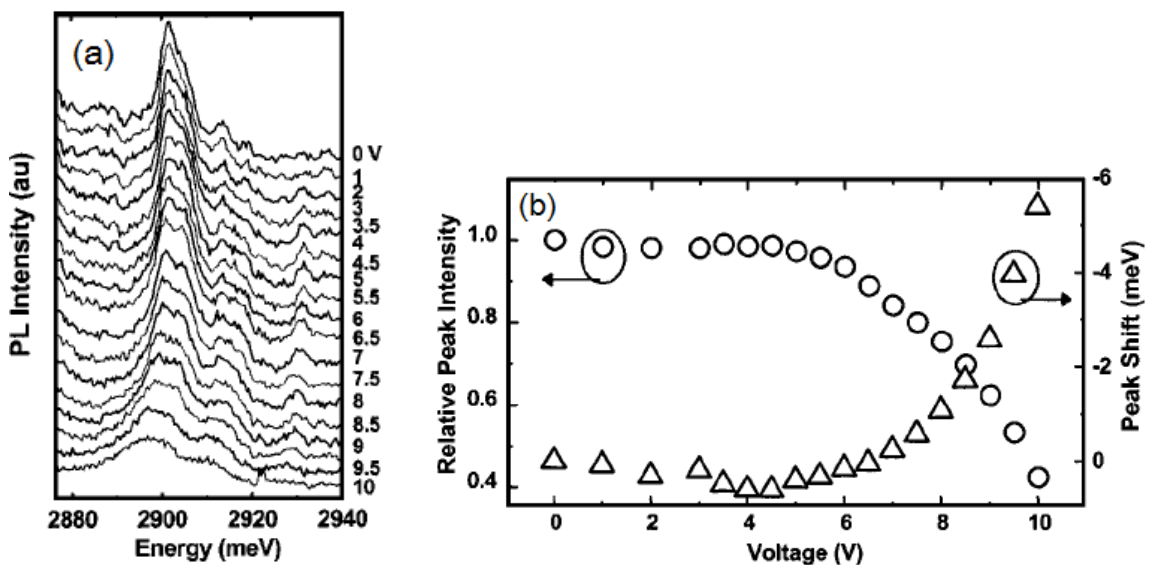


Figure 34. (a) Biased microPL spectra of a single InGaN layer grown on c-plane sapphire recorded at 4.2 K. (b) Plots of peak intensities and energies as a function of biases in (a).

Figure adopted from Ref. [55]

In order to observe a noticeable wavelength shift, the 2nd-generation samples were made and sent to University of Oxford, UK for low temperature (4.2K) biased microPL measurement. For the new samples, the gaps between adjacent metal pads were increased to 3 μm to improve the detection efficiency of the optical signals from QWs. The rest parts of the samples remained the same as those described in section 6.2.

Preliminary results from the new samples still exhibited no changes in energy shift as the lateral biases were increased to 20 V. The large surface leakage currents (> 0.1 A) were believed as the cause to the absence of energy shifts. For successful measurements, the surface currents should be less than 10 μA in the bias range of 0 ~ 20 V. The large surface leakage currents indicated that very limited potential drop was generated across the QWs. As a result, the carries in the QWs could not response to the electrical fields which were externally applied. In order to resolve the leakage problem, the 3rd-generation samples were planned.

6.4 Conclusions

Biased microPL measurements were performed on m-plane InGaN/GaN QWs with the attempt to investigate the possible internal fields induced by the polarization running across any dot-like structures in the InGaN layer. The results indicated that the externally applied biases were not sufficient to cause noticeable energy shifts of the QWs. It was believed that the strong surface leakage currents were responsible for the absence of energy shift.

CHAPTER 7

Summaries and Future Works

7.1 Summaries

M-plane bulk GaN sliced from c-plane GaN boules was regrown by HVPE with the attempt to increase substrate size. Substantial lateral regrowth rates ($> 250 \mu\text{m/hr}$) were observed in $[0001]$, $[11\bar{2}0]$ and $[\bar{1}120]$ directions. The 120° angle between the different facets shows the m-plane is one of the preferential expansion planes during the regrowth. The dislocation densities in the seed and the regrown areas were approximately $5 \times 10^6 \text{ cm}^{-2}$ and $1 \times 10^6 \text{ cm}^{-2}$, respectively. The high lateral regrowth rate and low dislocation density indicate a feasible method to obtain large-area, high-quality nonpolar GaN substrates.

GaN substrates with subsurface damages were treated with two different annealing conditions. The annealing with H_2 -containing gases at 950°C led to an inhomogeneous etching effect, and produced a substrate surface with more scratches and enhanced roughness. On the other hand, the annealing with NH_3 and N_2 at the same temperature resulted in a substrate surface with significantly reduced subsurface damages. Surface roughness and

optical properties of the sample were slightly sacrificed after the annealing with such gas mixtures. The depth of the subsurface damages was estimated by the CL images taken at different excitation voltages. The results indicated the damaged region was within 1.48 μm from the surface.

The effect of m-plane GaN substrates miscut angles on the properties of InGaN/GaN QWs were investigated. It was found that surface roughness and emission wavelengths of the QWs were highly sensitive to the miscut toward a-axis. With the miscut toward a-axis fixed at 0° , the changes in surface roughness and emission wavelength were limited when the miscut toward c-axis increased from 0.1° to 0.7° . As the miscut toward a-axis was increased to 0.1° , surface roughness was enhanced by 25 times and emission wavelength became longer by 45 nm when the miscut toward c-axis increased from 0.1° to 0.3° . The results indicated that the control range of m-plane QWs' properties can be significantly improved when the substrate miscut toward a-axis was slightly increased from 0° to 0.1° .

InGaN/GaN QWs grown on polar (c-plane) and nonpolar (m-plane) GaN substrates were studied theoretically and experimentally. Calculations based on stationary perturbation theory were performed to evaluate the influence of a static electrical field on a single InGaN/GaN QW. The results showed that emission-rate drop of 220 % and red-shift of 25 nm occurred when the electrical field increased from 0 to 1 MV/cm.

InGaN/GaN QWs were grown by MOCVD on c-plane and m-plane GaN substrates with comparable conditions. Lower emission intensities and longer peak wavelength were observed on c-plane QWs. This was attributed to the band tilting in c-plane QWs caused by QCSE in c-plane QWs. However, the intensity ratios (m-plane QWs to c-plane QWs)

decreased from 3.04 at 1 nA to 1.53 at 1000 nA. The observation was explained by the stronger screening effects of QCSE at higher current densities in c-plane QWs.

Biased microPL measurements were carried out on m-plane InGaN/GaN QWs. The purpose was to investigate the possible internal fields induced by the polarization running across any dot-like structures in the InGaN layer. The results of several initial trials indicated that the externally applied biases were not sufficient to cause noticeable energy shifts of the QWs. One of the possible causes was the strong surface leakage currents. In order to obtain detectable energy shifts under biases, new samples with modified layer structures have been proposed.

7.2 Future Works

The first thing to do is to successfully perform the biased microPL measurements with m-plane QWs. Any detectable energy shift, either $\Delta E > 0$ or $\Delta E < 0$, would be a direct evidence to show if there is any internal field induced in the “nonpolar” QWs. Figure 35 shows the layer structures planned for the 3rd-generation samples. A list of changes is shown below:

1. The QW periods will be reduced to 1 in order to receive clear optical signal from any dot-like structures. Emission characteristics of the 3-period InGaN/GaN layers would be slightly shifted relative to one another due to differences in the local strain. This would naturally lead to a smearing out around the spectral regions of interest.
2. The QW cap layer will be thinned from 50 nm to 7 nm to prevent current flowing.

3. The metal alloy will be Cr/Ni/Au, instead of Ti/Al. As the unintentionally-doped cap layer is slightly n-type, and Ti/Al is the alloy to make ohmic contact on n-GaN. To avoid excess carriers being injected to the epi-layer, Schottky contact (Cr/Ni/Au) to n-GaN will be used.
4. In order to prevent surface oxidation and any potential defects, which are likely to enhance leakage currents, an isolation layer of SiN will be deposited on the sample surface.

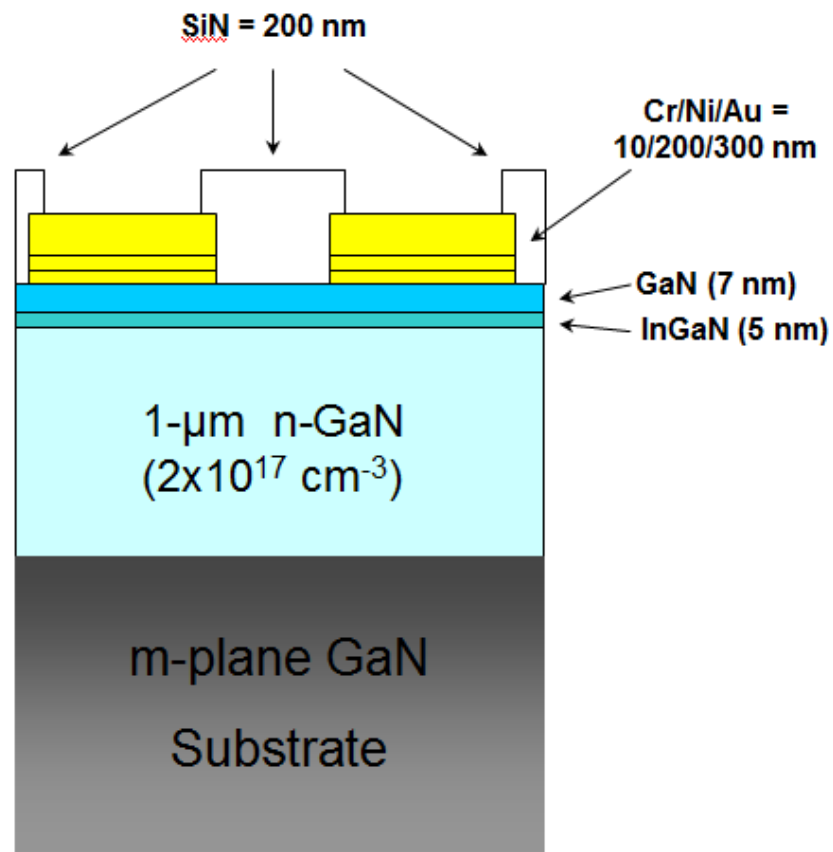
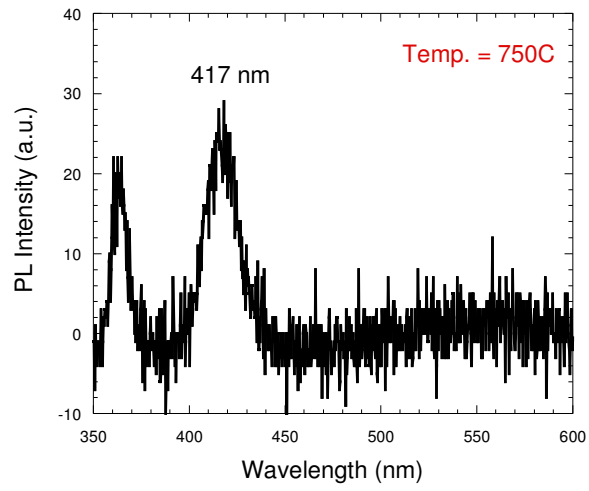


Figure 35. Layer structure of the 3rd-generation sample for biased microPL measurement.

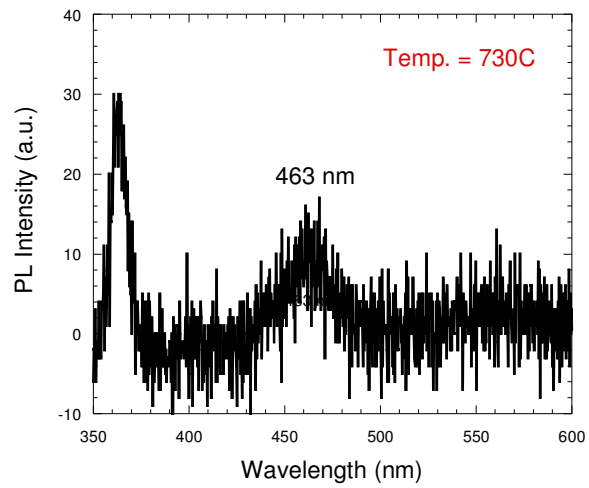
The second thing to follow up is to increase the emission wavelengths of nonpolar QWs. It is believed that nonpolar InGaN QWs will exhibit greater potential at longer emission wavelengths. Longer emission wavelengths require higher In incorporation efficiencies in the QWs, which results in stronger piezoelectric polarization due to the increase in lattice mismatch between well and barrier. As larger internal fields will be induced by the stronger piezoelectric polarization, nonpolar QWs are expected to bring more improvement in the luminous efficiencies of InGaN-based QWs.

Higher In incorporation efficiencies are typically achieved by lower growth temperatures or higher TMIn flow rates. In the process of increasing QW peak wavelengths, the trade-off between In compositions and crystal qualities should always be considered. Figure 36 shows the PL spectra of the InGaN QWs grown on sapphire at different growth temperatures. It can be seen that lowering the QW growth temperature from 750°C to 730°C increased the peak wavelength from 417 nm to 463 nm, but the emission intensity decreased by ~50%. The result indicated that the carrier confinement of a QW structure deteriorated at the lower growth temperature.

Figure 37 shows PL spectra of the QWs grown at different TMIn flows. As shown in the figure, the emission wavelength was increased from 441 nm to 483 nm when TMIn flow increased from 38 sccm to 45 sccm. However, this was also achieved at the sacrifice of emission intensity. Increasing TMIn flows in the QW may not only bring up the In composition, but also increase the QW width. As In composition and QW width increase, the strain energy in active region also increases, and this will introduce additional defects in the epitaxial film.

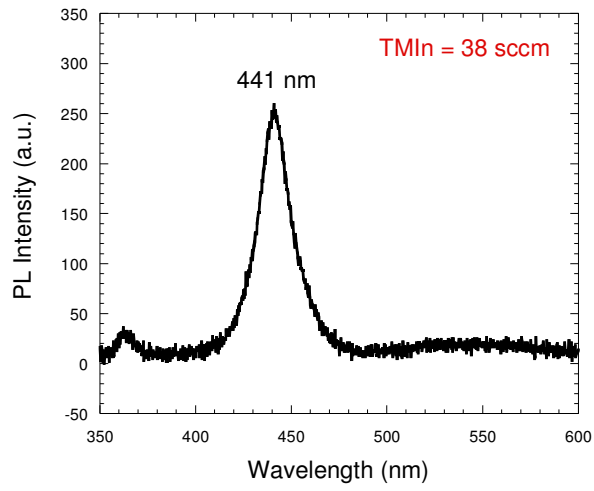


(a)

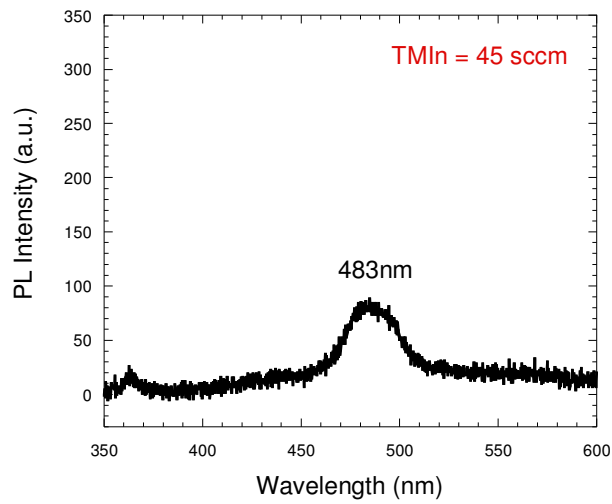


(b)

Figure 36. PL spectra of the InGaN/GaN QWs grown on sapphire at the growth temperature of (a) 750°C and (b) 730°C. The peaks at 362 nm were from the near-band-edge emission of GaN.



(a)



(b)

Figure 37. PL spectra of the InGaN/GaN QWs grown on sapphire at the TMI flow of (a) 38 sccm and (b) 45 sccm.

Bibliography

1. N. Holonyak, Jr. and S. F. Bevacqua, *Appl. Phys. Lett.* **1**, 82, 1962.
2. M.G. Craford, Roger W. Shaw, A.H. Herzog, and W.O. Groves, *J. Appl. Phys.* **43**, 4075, 1972.
3. M.G. Craford, *IEEE circuit Devices* **8**, 25, 1992.
4. J.I. Pankove, *J. Luminescence* **4**, 63, 1971.
5. K. Hiramatsu, S. Itoh, H. Amano, I. Akasaki, N. Kuwano, T. Shiraishi, and K. Oh, *J. Cryst. Growth* **115**, 628, 1991.
6. S. Nakamura, *Jpn. J. Appl. Phys.* **30**, L1705, 1991.
7. H. Amano, M. Kito, K. Hiramatsu, I. Akasaki, *Jpn. J. Appl. Phys.* **28**, L2112, 1989.
8. S. Nakamura, T. Mukai, M. Senoh, *Jpn. J. Appl. Phys.* **30**, L1998, 1991.
9. Figure available at
<http://www.aps.org/meetings/multimedia/march2007/upload/craford.pdf>.
10. I. Akasaki, K. Hiramatsu, and H. Amano, *Memoirs of the faculty of Engineering, Nagoya University*, **43**, 147, 1991.
11. S.D. Lester, F.A. Ponce, M.G. Craford, and D.A. Steigerwald, *Appl. Phys. Lett.* **66**, 1249, 1995.
12. I. Ho and G.B. Stringfellow, *Appl. Phys. Lett.* **68**, 2701, 1996.
13. S. Chichibu, T. Azuhata, T. Sota, and S. Nakamura, *Appl. Phys. Lett.* **70**, 2822, 1997.
14. Y. Narukawa, Y. Kawakami, M. Funato, S. Fujita, S. Fujita, and S. Nakamura, *Appl. Phys. Lett.* **70**, 981, 1997.

15. K.P. O'Donnell, R.W. Martin, and P.G. Middleton, *Phys. Rev. Lett.* **82**, 237, 1999.
16. I.L. Krestnikov, N.N. Ledentsov, A. Hoffmann, D. Bimberg, A.V. Sakharov, W.V. Lundin, A.F. Tsatsul'nikov, A.S. Usikov, Zh. I. Alferov, Yu. G. Musikhin, and D. Gerthsen, *Phys. Rev. B* **66**, 155310, 2002.
17. H. Fujikura, K. Lizuka, and S. Tanaka, *Jpn. J. Appl. Phys.* **42**, 2767, 2003.
18. A.D. Williams, T.D. Moustakas, *J. Crystal Growth* **300**, 37, 2007.
19. K. Akita, T. Kyono, Y. Yoshizumi, H. Kitabayashi, and K. Katayama, *J. Appl. Phys.* **101**, 033104, 2007.
20. X.A. Cao, H. Lu, E.B. Kaminsky, S.D. Arthur, J.R. Grandusky, and F. Shahedipour-Sandvik, *J. Crystal Growth* **300**, 382, 2007.
21. K. Motoki *et al.*, *Jpn. J. Appl. Phys.* **40**, L140, 2001.
22. Image available at http://www.sei.co.jp/sei_info_e/pdf/profile_e.pdf
23. F. Bernardini and V. Fiorentini, *Phys. Stat. Sol. (b)* **216**, 391, 1999.
24. F. Bernardini and V. Fiorentini, *Phys. Rev. B* **56**, R10024, 1997.
25. T. Takeuchi, H. Amano, and I. Akasaki, *Jpn. J. Appl. Phys.* **39**, 413, 2000.
26. T. Takeuchi, S. Sota, M. Katsuragawa, M. Komori, H. Takeuchi, H. Amano, and I. Akasaki, *Jpn. J. Appl. Phys.* **36**, L382, 1997.
27. D. A. B. Miller, D. S. Chemla, T. C. Damen, A. C. Gossard, W. Wiegmann, T. H. Wood, and C. A. Burrus, *Phys. Rev. Lett.* **53**, 2173, 1984.
28. B. A. Haskell, A. Chakraborty, F. Wu, H. Sasano, P. T. Fini, S. P. DenBaars, J. S. Speck, and S. Nakamura, *J. Electron Material* **34**, 357, 2005.

29. M. D. Craven, S. H. Lim, F. Wu, J. S. Speck, and S. P. DenBaars, *Appl. Phys. Lett.* **81**, 469, 2002.
30. C. Q. Chen, V. Adivarahan, M. Shatalov, M. E. Gaevski, E. Kuokstis, J. W. Yang, H. P. Maruska, Z. Gong, M. A. Khan, R. Liu, A. Bell, F. A. Ponce, *phys. stat. sol. (c)* **2**, 2732, 2005.
31. T. Paskova, R. Kroeger, S. Figge, D. Hommel, V. Darakchieva, B. Monemar, E. Preble, A. Hanser, N. M. Williams, and M. Tutor, *Appl. Phys. Lett.* **89**, 051914, 2006.
32. K. Okamoto, H. Ohta, D. Nakagawa, M. Sonobe, J. Ichihara and H. Takasu, *Jpn. J. Appl. Phys.* **45**, L1197, 2006.
33. K. Okamoto, H. Ohta, S. F. Chichibu, J. Ichihara, and H. Takasu, *Jpn. J. Appl. Phys.* **46**, L187, 2007.
34. J.R. Grandusky, V. Jindal, N. Tripathi, F. Shahedipour-Sandvik, H. Lu, E.B. Kaminsky, and R. Melkote, *J. Crystal Growth* **307**, 309, 2007.
35. J.H. Ryu, D.K. Oh, S.T. Yoon, B.G. Choi, J.-W. Yoon, and K.B. Shim, *J. Crystal Growth* **292**, 206, 2006.
36. A. Koukitu, S. Hama, T. Taki and H. Seki, *Jpn. J. Appl. Phys.* **37**, 762, 1998.
37. Software available at [http:// www.gel.usherbrooke.ca/casino](http://www.gel.usherbrooke.ca/casino).
38. The main difference in growth conditions for Sample A and Sample B were oxygen and ammonia flows. The oxygen flow ratio for Sample A and B is 4:1, while the ammonia flow ratio is 1:3. Oxygen was used for n-type doping. Ammonia was used to provide nitrogen source.

39. G.A. Slack, L.J. Schowalter, D. Morelli, and J.A. Freitas Jr., *J. Crystal Growth* **246**, 287, 2002.
40. M.E. Vickers, M.J. Kappers, T.M. Smeeton, E.J. Thrush, J.S. Barnard, and C.J. Humphreys, *J. Appl. Phys.* **94**, 1565, 2003.
41. H. Yamada, K. Iso, M. Saito, H. Hirasawa, N. Fellows, H. Masui, K. Fujito, J.S. Speck, S.P. DenBaars, and S. Nakamura, *Phys. Stat. Sol. (RRL)* **2**, 89, 2008.
42. K.-C. Kim, M.C. Schmidt, H. Sato, F. Wu, N. Fellows, M. Saito, K. Fujito, J.S. Speck, S. Nakamura, and S.P. Denbaars, *phys. stat. sol. (RRL)* **1**, 125, 2007.
43. H. Yamada, K. Iso, H. Masui, M. Saito, K. Fujito, S.P. DenBaars, and S. Nakamura, *J. Crystal Growth* **310**, 4968, 2008.
44. M.C. Schmidt, K.-C. Kim, H. Sato, N. Fellows, H. Masui, S. Nakamura, S.P. Denbaars, and J.S. Speck, *Jpn. J. Appl. Phys.* **46**, L126, 2007.
45. T. Detchprohm, M. Zhu, Y. Li, Y. Xia, C. Wetzel, E.A. Preble, L. Liu, T. Paskova, and D. Hanser, *Appl. Phys. Lett.* **92**, 241109, 2008.
46. K. Iso, H. Yamada, H. Hirasawa, N. Fellows, M. Saito, K. Fujito, S.P. DenBaars, J.S. Speck, and S. Nakamura, *Jpn. J. Appl. Phys.* **46**, L960, 2007.
47. C. Mion, PhD dissertation, “*Investigation of the thermal properties of gallium nitride using the three omega technique*”, North Carolina State University, pp. 51, 2005.
48. C. Mion, J.F. Muth, E.A. Preble, and D. Hanser, *Mat. Res. Soci. Symp. Proc.* **892**, 0892-FF29-05.1, 2006.
49. H. Sakuta, Y. Kawano, Y. Yamanaka, S. Kurai, and T. Taguchi, *Phys. Stat. Sol. (c)* **2**, 2407, 2005.

50. H. Kroemer, “*Quantum Mechanics*”, Prentice Hall, p516-517, 1994.
51. T. Mukai, M. Yamada, and S. Nakamura, *Jpn. J. Appl. Phys.*, Part 1 **38**, 3976, 1999.
52. Y.C. Shen, G.O. Mueller, S. Watanabe, N.F. Gardner, A. Munkholm, and M.R. Krames, *Appl. Phys. Lett.* **91**, 141101, 2007.
53. J. Xie, X. Ni, Q. Fan, R. Shimada, U. Ozgur, and H. Morkoc, *Appl. Phys. Lett.* **93**, 121107, 2008.
54. S.-H. Park and S.-L. Chuang, *Phys. Rev. B* **59**, 4725, 1999.
55. J.W. Robinson, J.H. Rice, K.H. Lee, J.H. Na, R.A. Taylor, D.G. Hasko, R.A. Oliver, M.J. Kappers, C.J. Humphreys, and G.A.D. Briggs, *Appl. Phys. Lett.* **86**, 213103, 2005.
56. A.F. Jarjour, R.A. Oliver, A. Tahraoui, M.J. Kappers, C.J. Humphreys, and R.A. Taylor, *Phys. Rev. Lett.* **99**, 197403, 2007.
57. T.H. Myers, B.L. VanMil, L.J. Holbert, C.Y. Peng, C.D. Stiespring, J. Alam, J.A. Freitas Jr., V.A. Dmitriev, A. Pechnikov, Y. Shapovalova, and V. Ivantsov, *J. Crystal Growth* **246**, 244, 2002.
58. M.A. Mastro, O.M. Kryliouk, M.D. Reed, T.J. Anderson, A. Davydov, and S. Shapiro, *phys. stat. sol. (a)* **188**, 467, 2001.
59. H. Shin, E. Arkun, D.B. Thomson, P. Miraglia, E. Preble, R. Schlessler, S. Wolter, Z. Sitar, and R.F. Davis, *J. Crystal Growth* **236**, 529, 2002.

Appendices

Appendix A

MATLAB Code: Calculations of Quantum-confined Stark Effect in a Single $\text{In}_{0.15}\text{Ga}_{0.85}\text{N}/\text{GaN}$ Quantum Well

```
clear all;
```

```
echo off;
```

```
m0 = 9.1e-31; (free electron mass, Kg)
```

```
h = 1.05e-34; (Plank constant, J-s)
```

```
x=0.15; (Indium content)
```

```
Eg=3390*(1-x)+650*x; (Band gap energy of  $\text{In}_x\text{Ga}_{1-x}\text{N}$ , meV)
```

```
L = 6e-9; (quantum well width)
```

```
V0 = 430*x*1.6*1e-22; (Conduction Band offset, meV)
```

```
V0h = 1000*x*1.6*1e-22; (Valence Band offset, meV)
```

```
m = (0.2*(1-x)+0.11*x)*m0; (electron effective mass of  $\text{In}_x\text{Ga}_{1-x}\text{N}$ )
```

```
mh = (1.5*(1-x)+1.63*x)*m0; (heavy hole effective mass of  $\text{In}_x\text{Ga}_{1-x}\text{N}$ )
```

```
theta0= sqrt((m*V0*L^2)/(2*h^2));
```

```
theta0h= sqrt((mh*V0h*L^2)/(2*h^2));
```

```
theta = 0:0.001:pi;
```

```
f=sqrt(((theta0./theta).^2)-1);
```

```
t=tan(theta);
```

```
tt=-cot(theta);
```

```
d=abs(f-t);
```

```
dd=abs(f-tt);
```

```
fh=sqrt(((theta0h./theta).^2)-1);
```

```
th=tan(theta);
```

```
tth=-cot(theta);
```

```
dh=abs(fh-t);
```

```
ddh=abs(fh-tth);
```

Solving Schrodinger equation

with finite barrier potential

```
figure(1);
```

```
subplot(2,1,1);
```

```
plot(theta,t,theta,f,theta,tt);
```

```
AXIS([0 pi 0 5]);
```

```
title('Boundary Solutions in Conduction Band');
```

```
xlabel('\theta = kL / 2');
```

```

subplot(2,1,2);

plot(theta,t,theta,fh,theta,tt);

title('Boundary Solutions in Valence Band');

xlabel('\theta = kL / 2');

AXIS([0 pi 0 15]);

for i=1:length(d)
    if d(i) == min(d)
        n = i;
    end
    if dd(i) == min(dd)
        p = i;
    end
    if dh(i) == min(dh)
        nh = i;
    end
    if ddh(i) == min(ddh)
        ph = i;
    end
end
end

```


 Obtaining the first 2 bound energy states in conduction band and in valence band.

```

theta1 = theta(n);
theta2 = theta(p);
k1 = 2*theta1/L;
k2 = 2*theta2/L;
E1 = h*h*k1*k1/(2*m*1.6e-22)
E2 = h*h*k2*k2/(2*m*1.6e-22)

```

```

theta1h = theta(nh);
theta2h = theta(ph);
k1h = 2*theta1h/L;
k2h = 2*theta2h/L;
E1h = h*h*k1h*k1h/(2*mh*1.6e-22)
E2h = h*h*k2h*k2h/(2*mh*1.6e-22)

```

Obtaining the first 2 bound energy states in conduction band and in valence band.

```

e=0.01:0.01:1;
E0=e*500;

c1_sq=8*theta1/(4*theta1*L-L*sin(4*theta1));
c2_sq=8*theta2/(4*theta2*L+L*sin(4*theta2));
Rr=c1_sq.*E0*L*(0.25-(1-
    cos(4*theta1))/(32*theta1*theta1));

```

Calculating the perturbed energy eigenstates.

```

alpha=k1+k2;
beta=k1-k2;
S=-0.5*sqrt(c1_sq*c2_sq).*E0*(-cos(alpha*L)/alpha+
    sin(alpha*L)/L/alpha/alpha-cos(beta*L)/beta+
    sin(beta*L)/L/beta/beta-(1-cos(alpha*L))/alpha-
    (1-cos(beta*L))/beta);
U=c2_sq.*E0*(L/4-(cos(2*k2*L)-1)/8/k2/k2/L);
b=E1+E2+Rr+U;
c=(E1+Rr).*(E2+U)-S.*S;
E1p=0.5.*(b-sqrt(b.*b-4.*c));
E2p=0.5.*(b+sqrt(b.*b-4.*c));
ratio=-S./(E1+Rr-E1p);
A=ratio./(abs(ratio)+1);
B=1./(abs(ratio)+1);

```

Calculating the perturbed energy eigenstates.

```

c1_sqh=8*theta1h/(4*theta1h*L-L*sin(4*theta1h));
c2_sqh=8*theta2h/(4*theta2h*L+L*sin(4*theta2h));
Rh=-c1_sqh.*E0*(L/4-L*(1-
    cos(4*theta1h))/32/theta1h/theta1h);
alphah=k1h+k2h;
betah=k1h-k2h;
Sh=0.5*sqrt(c1_sqh*c2_sqh).*E0*(-

```

Obtaining the wavefunctions for electrons and holes.

```

cos(alphah*L)/alphah+
sin(alphah*L)/L/alphah/alphah-
cos(betah*L)/betah+
sin(betah*L)/L/betah/betah-(1-
cos(alphah*L))/alphah-(1-
cos(betah*L))/betah);
Uh=-c2_sqh.*E0*(L/4-(cos(2*k2h*L)-
1)/8/k2h/k2h/L);
bh=E1h+E2h+Rh+Uh;
ch=(E1h+Rh).*(E2h+Uh)-Sh.*Sh;
E1ph=0.5.*(bh-sqrt(bh.*bh-4.*ch));
E2ph=0.5.*(bh+sqrt(bh.*bh-4.*ch));
ratioh=-Sh./(E1h+Rh-E1ph);
Ah=ratioh./(abs(ratioh)+1);
Bh=1./(abs(ratioh)+1);

```

Obtaining the wavefunctions
for electrons and holes.

```

for z=1:length(e)
    E1_plot(z)=E1;
    E2_plot(z)=E2;
    E1h_plot(z)=E1h;
    E2h_plot(z)=E2h;
end

```

```

figure(2);

plot(e,E1_plot,e,E2_plot,e,E1p,e,E2p);

title('The first 2 states in CB')

xlabel('Electric Fields (MV/cm)');ylabel('Energy (meV)');

figure(3);

plot(e,-E1h_plot,e,-E2h_plot,e,-E1ph,e,-E2ph);

title('The first 2 states in VB')

xlabel('Electric Fields (MV/cm)');ylabel('Energy (meV)');

figure(4);

plot(e,Ah,e,Bh);

```

```

dx=0.1;
x=0:dx:L*1e10;
ph1=sqrt(c1_sq)*(1e-10).*sin(k1.*x*1e-10);
ph2=sqrt(c2_sq)*(1e-10).*cos(k2.*x*1e-10);
ph1h=sqrt(c1_sqh)*(1e-10).*sin(k1h.*x*1e-10);
ph2h=sqrt(c2_sqh)*(1e-10).*cos(k2h.*x*1e-10);
for k=1:length(x)
    r_nor(k)=ph1(k)*x(k)*ph1h(k)*dx;
end
RR_nor=sum(r_nor)^2;

```

Calculating the spontaneous
emission rates

```

for j=1:length(E0)
    for k=1:length(x)
        phe(j,k)=A(j)*ph1(k)+B(j)*ph2(k);
        phh(j,k)=Ah(j)*ph1h(k)+Bh(j)*ph2h(k);
        r(j,k)=phe(j,k)*x(k)*phh(j,k)*dx;
    end
    R(j)=sum(r(j,:));
    RR(j)=abs(R(j))^2;
End

```

} Calculating the spontaneous
emission rates

```

figure(5);
subplot(3,1,1);
plot(x,2+phe(10,:)*1e6,x,-1+phh(1,:)*1e6);
axis([0 60 -5 5]);
title('The Wavefunctions at E_0 = 0.01MV/cm')
subplot(3,1,2);
plot(x,2+phe(50,:)*1e6,x,-1+phh(50,:)*1e6);
axis([0 60 -5 5]);
title('The Wavefunctions at E_0 = 0.5MV/cm')
subplot(3,1,3);
plot(x,2+phe(90,:)*1e6,x,-1+phh(100,:)*1e6);

```

```

axis([0 60 -5 5]);
title('The Wavefunctions at E_0 = 1MV/cm')
xlabel('Distance (A)');
figure(6);
plot(e,RR/RR_nor)
xlabel('Electric Fields (MV/cm)');
ylabel('Normalized Spontaneous Emission Rate');

del_E=Eg+E1p+E1ph;
lenda=1240000./del_E;
figure(7);
plot(e,lenda);
xlabel('Electric Fields (MV/cm)');
ylabel('Wavelength (nm)');

```

Appendix B

MOCVD Operation Procedures

1. Transfer Sample Block (SB) into the chamber.
2. Lower SB down.
3. Close shutters.
4. Close the LL-MC (Load Lock Main Chamber) Gate Valve.
5. Set Rotation Speed to 1100 RPM.
6. Send Rotation Speed.
7. Close Turbo Pump gate valve (Green to Red).
8. Select “send valve settings”.
9. Open Mechanical Valve (Red to Green)
10. Select “send valve settings”.
11. Turn on H₂ Purifier(see procedure)
12. Check H₂ cylinder in Room 108GC.
 - A. Make sure valve is open.
 - B. Check Cylinder pressure (uses ~350psi/Hr).
13. Check Ammonia Cylinder.
 - A. Check weight, new cylinder weighs ~50lbs.
 - B. Change cylinder when <10lbs.
14. Check N₂ UC (Ultra Carrier) process cylinder in Room 109.
 - A. When growing GaN 500psi is O.K (depends on growth time).
 - B. When growing AlGaIn, need more than 500 psi.
15. Fill out Run sheet.
16. Check bubbler water levels.
17. Check MKS Pressure Controller for 0 settings (Need not do this everytime)
 - A. Press any key, screen will light up
 - B. Press right arrow key
 - C. Execute is selected.
 - D. Press down arrow key.

- E. Display reads Done.(Done means zeroed)
 - F. Go to channel 2, Press right arrow key.
 - G. Execute is selected.
 - H. Press arrow down key
 - I. Display reads done.
 - J. Repeat Process for every channel, 1-8.
- *CH6 not connected, displays fail for bubbler pressure controller.
18. MO (Metal Organic) source control Panel on computer display shows the pressure at 0 (Not used now).
 19. Close all by-pass valves (top) by clicking on them.
 20. Select send valve settings.
 21. Open Ammonia by-pass valve.
 22. Select send valve settings.
 23. Open MO carrier by-pass valve.
 24. Select send valve settings.
 25. Open H2 by-pass valve.
 26. Select send valve settings.
 27. Set Bps line Purge Flow to 200 sccm.
 28. Set Ferrofulidic Feed through Purge to 150 sccm.
 - 28-A: Select "send flow rates".
 - 28-B: Select "send valve settings".
 29. Set View port Purge to 150 sccm.
 - 29-A: Select "send flow rates".
 - 29-B: Select "send valve settings".
 30. Set Transfer Purge to 150sccm.
 - 30-A: Select "send flow rates".
 - 30-B: Select "send valve settings".
 31. Set Pyrometer Purge to 150sccm.
 - 31-A: Select "send flow rates".
 - 31-B: Select "send valve settings".
 32. Set Turbo Pump Purge to 200sccm.
 - 32-A: Select "send flow rates".
 - 32-B: Select "send valve settings".
 33. Set the Chamber Purge N₂ to 1,000 sccm.
 34. Set the Chamber Purge H₂ to 1,000sccm.
- Note: Chamber Purge N₂&H₂ are flashing.

35. Select Send Flow Rates.
36. Select Send Valve Settings.
37. Set chamber purge N₂ and H₂ to 5000 sccm by increments of 1000 sccm and “sending” flow rates at each increment.
38. Set Chamber Pressure to 50 Torr.
39. Set Bps Line Pressure to 20 Torr.
40. Select Send Pressure.
41. Set Ammonia flow to 750sccm.
42. Click mouse anywhere in gray area.
43. Ammonia Valve is flashing.
44. Select “Send Flow Rates”.
45. Select “Send Valve Settings”.
46. Open the chamber valve for Ammonia.
47. Close the by-pass valve for Ammonia.
48. Select Send Valve Settings.*****
49. Set H₂ to 1000sccm.
50. Click mouse in gray area.
51. Select “Send Flow Rates”.
52. Select “Send Valve Settings”.
53. Open the chamber valve for H₂.
54. Close the bypass valve for H₂.
55. Select “Send Valve Settings”.
56. Set H₂ to 5250sccm by increments of 1,000sccm by “sending” flow rates at each increment.
57. Set MO Car/H₂ to 700sccm.
58. Click Mouse in Gray Area.
59. Select “Send Flow Rates”.
60. Select “Send Valve Settings”.
61. Open the MO Car/H₂ chamber valve.
62. Close the MO Car/H₂ By-Pass valve.
63. Select “Send Valve Settings”.
64. Start Heating SB by selecting “Send Temperature”.
 Increase Bottom Sorensen Power Supply to 2.5amps.
 Increase Top Sorensen Power Supply to 2.5amps.
 Increase Bottom Sorensen Power Supply to 5.0amps.
 Increase Top Sorensen Power Supply to 5.0amps.

- Increase Bottom Sorensen Power Supply to 10.0amps.
- Increase Top Sorensen Power Supply to 10.0amps.
- Increase Bottom Sorensen Power Supply to 15amps.
- Increase Top Sorensen Power Supply to 15amps.
- Increase Bottom Sorensen Power Supply to 20amps.
- Increase Top Sorensen Power Supply to 20amps.
- Increase Bottom Sorensen Power Supply to 25amps.
- Increase Top Sorensen Power Supply to 24amps.
- 65. Wait until zone 1 set point reads to 500°C.
- 66. Wait until zone 2 set point reads to 1100°C.
- 67. When the current LED turns off on the Top Sorensen Power Supply, and the voltage LED turns on adjust the current control to Maximum on the inner filament (top unit).
- 68. Set “Zone 1” to 1000 °C.
- 69. Select “Send Temperature”.
- 70. Zones 1 and 2 start ramping up.
- 71. Adjust the bottom Sorensen Power Supply Current up keeping it about the same power with the top Sorensen Power Supply until you reach 52 amps.
- 72. When “Zone 1” reaches set point (not actual temperature) log Preheat Time on Run Sheet. Preheat for 10 minutes.
- 73. Set up while Preheat is running.
 - A. Set TMA1 Pressure to 760 Torr on MO Source Control Panel.
 - B. Send Pressure on MO Source Control Panel.
 - C. Open TMA1/H2 By-Pass Valve (starts flashing).
 - D. Select Send Valve Settings.
 - E. Open TMA Car/H2 By-Pass Valve (starts flashing).
 - F. Select Send Valve Settings.
 - G. Set TMA1/H2 to 30sccm.
 - H. Set TMA1 Car/H2 Valve to 60sccm.
 - I. Click mouse in gray area (flashing).
 - J. Select Send Flow Rates.
 - K. Select Send Valve Settings.
- 74. Set zone 1 to 500 °C; Set Chamber Pressure to 20 Torr.
- 75. When Preheat is finished:
 - A. Select Send Temperature.
 - B. Select Send Pressure.
 - C. Start timer

76. Adjust the current on the bottom Sorensen Power Supply Keeping the power on the top and bottom the same. (This step will be slow as the powers decrease slowly).
77. Adjust the bottom Sorensen Power Supply Current to 23.2 amps.
78. Click on TMAI/H2 and TMAI Car/H2 By-Pass and chamber Injection valves. (Valves are flashing).
79. When 7 minutes is up and the temperature is 498-500°C, select "Send Valve Settings".
80. LT-Buffer Layer is growing.
81. While the buffer layer is growing, click on TMAI/H2 and TMAI Car/H2 By-Pass and Chamber Injection Valves.
82. Set Chamber Pressure to 30 Torr. It should be 76 Torr for GaN.
83. Set Substrate temperature of "Zone 1" to 1120 °C (for AlGaIn). This temperature varies depending on the film being grown.
84. When LT-Buffer Layer is finished, select "Send Valve Settings".
Note: 7:30' minutes time starts. This varies depending on the final temperature setting, i.e; will be less for 1040 (7min) compared to 1120.
85. Select "Send Temperature".
86. Select Send Pressure.
87. Adjust the bottom Sorensen Power Supply Current to 60 amps. Adjust slowly keeping the same power between top and bottom units.
88. On the MO Source Control Panel set TEGa pressure to 760Torr.
89. Select Send Pressure on MO Source Control Panel.
90. Click on TEGa/H2 By-Pass Valve.
91. Select "Send Valve Setting".
92. Set TEGa/H2 to 30sccm (Flow rate set according to the Al composition).
93. Select "Send flow Rate".
94. Select "Send Valve Settings".
95. Set TMAI/H2 flow rate to 18 sccm. (Flow rate set according to the Al composition).
96. Select "Send flow Rate".
97. Click on TEGa/H2, TMAI/H2, and TMA Car/H2 valves, both By-Pass and Chamber Injection.(flashing).
98. When Zone 1 reaches 1120 °C and time is right(7: 30' minutes), go to next step. Log time on Run Sheet.
99. Select, Send Valve Settings.

100. Deposition started. * Note: set up 101-103 before finishes.
101. Click on TEGa/H2 By-Pass and chamber Injection valves.
102. Click on TMAI/H2 By-Pass and Chamber Injection valves.
103. Click on TMA Car/H2 By-Pass and Chamber Injection valves.
104. Set "Zone 1" to 500 °C.
105. When deposition finished:
 - A. Select "Send Valve Settings".
 - B. Select, "Send Temperature".

**** Steps 115, and 106-114 usually are done simultaneously ****

106. Set TEGa /H2 Flow Rate to 0. (flashing).
107. Set TMAI /H2 Flow Rate to 0. (flashing).
108. Set TMA Car/H2 Flow Rate to 0. (flashing).
109. Select "Send Valve Settings".
110. Select "Send Flow Rates".
111. Set TMAI Pressure (MO Source Control Panel) to 0.
112. Select "Send Pressure" (MO control panel).
113. Set TEGa Pressure (MO source control panel) to 0.
114. Select "Send Pressure" (MO source control panel).
115. Decrease current on the bottom Sorensen Power Supply slowly keeping the same ratio with the top unit.
116. When "Zone 2" is below 350 °C:
 - A. Click on Ammonia Chamber Valve.
 - B. Click on Ammonia By-Pass Valve.
 - C. Select "Send Valve Settings".
 - D. Set Ammonia Flow to 0.
 - E. Select "Send Valve Settings".
 - F. Select "Send Flow Rates".
117. Set Rotation Speed to 10 RPM.
118. Select "Send Rotation Speed".
119. Close H2 Valves as Following:
 - A. Click on H2 Chamber Injection Valve.
 - B. Click on H2 By-Pass Valve.
 - C. Select "Send Valve Settings".
 - D. Set H2 Flow Rate to 0.
 - E. Select "Send Valve Settings".
 - F. Select "Send Flow Rates".

120. Close MO Car/H2 Valves as following:
 - A. Click on MO Car/H2 Flow Rate to 0.
 - B. Click on MO Car/H2 By-Pass Valve.
 - C. Select "Send Valve Settings".
 - D. Set MO Car/H2 Flow Rate to 0.
 - E. Select "Send Valve Settings".
 - F. Select "Send Flow Rates".
121. Set Chamber Pressure to 0.
122. Set Bps Line Pressure to 0.
123. Select "Send Pressure".
124. Set Chamber Purge N2 and H2 to 0.
125. Select "Send Valve Settings".
126. Select "Send Flow Rates".
127. Close all purge N₂ lines by the following steps:
 - 127-A. Set View port purge to 0.
 - 127-B. Select, "send valve settings"
 - 127-C. Select, "send flow rates".
 - 127-D. Follow the same procedure for closing other purges.

Note: The Ferrofluidic Feedthru Purge and the By-Pass Line Purge Flow valves are changed together.
128. When Chamber Pressure =0, proceed to step 129.
129. Close the Mechanical Pump Valve (Process Pump).
130. Select "Send Valve Settings".
131. Turn Off Turbo Chamber IG.
132. Click on the Turbo Pump Valve.
133. Select "Send Valve Settings".
134. Wait until the Turbo pump valve opens.
135. Turn on Turbo chamber IG.
136. Set Rotation Speed to 0.
137. Select "Send Rotation Speed".
138. Remove Sample Block From Chamber.
139. Shut down H2 purifier, see Purifier Shut Down Procedure.
140. Open all By-Pass Valves.